SURFACE STUDIES OF NEW ANTI-FOULING POLYMERS BY SUM FREQUENCY GENERATION VIBRATIONAL SPECTROSCOPY

By

Cornelius Bruce Kristalyn

A dissertation submitted in partial fulfillment
of the requirements for the degree of
Doctor of Philosophy
(Chemistry)
in The University of Michigan
2010

Doctoral Committee:
Professor Zhan Chen, Chair
Professor Mark E. Meyerhoff
Professor Roseanne J. Sension
Associate Professor Shuichi Takayama

To Mom and Dad

ACKNOWLEDGEMENTS

The work presented in this thesis would not have been possible at all without the support and guidance of my research advisor Zhan Chen. I greatly appreciate the time he spent to help me develop as a scientist. He has not only been there to guide me when I needed, it but also let me progress on my own. The time spent working for Zhan was a wonderful experience which I will take with me for the rest of my life.

I would also like to thank Professors Meyerhoff, Sension, and Takayama for being on my committee. I am very thankful that they all took time out of their busy schedules to help me with my doctoral degree.

My lab mates have been a great support to me throughout my years at Michigan. Starting with my first years in the lab when Dr. Matt Clarke, Dr. Xiaoyun Chen, and Dr. Jie Wang took the time to help a new student learn the techniques and how to run the experiments. Continuing during my time here there have been many people who have grown with me as a researcher: Anne Vázquez, Chris Avery, Dr. Arthur McClelland, Sarah Spanninga, and Andy Boughton. Having lab mates who were there to pick me up when I fell down was a great help, as well as having someone to talk to when I was thinking through problems. All members of the Chen lab both past and present, have been a great group to work with and I thank them all for helping me in all the different individual ways.

A large part of this thesis would not have been possible without the collaboration of Dr. Christopher Ober at Cornell University. His students, Sitaraman Krishnan, Craig J. Weinman, Harihara S. Sundaram, and Younjin Cho, have all been of great help as I worked to analyze the polymers they sent to us over the years. Without their efforts to develop these materials, none of my work would have been possible.

I am extremely grateful for the support from the Office of Naval Research. Funding provided by them has supported me for much of my graduate career as well as helped to supply me with the resources necessary to complete this work.

Most importantly, I am happy to thank my family and friends without whom I would never have progressed. My parents have always been there for me and pushed me to achieve even when I lacked the desire. My brothers and friends have been wonderful for providing companionship and distractions to help me realize that there is always more to life than just the next pieces of the current project.

TABLE OF CONTENTS

LIST OF FIGURES

LIST OF TABLES

CHAPTER 1: INTRODUCTION

1.1 MOTIVATION

Biofouling has long been a problem with marine vessels.[1] The accumulation of biofoulants on ship hulls results in a decrease in operational speed as well as an increase in fuel costs due to increased hydrodynamic drag. Anti-fouling coatings traditionally have included biocides that are released into the marine environment, which have a negative impact on non-target organisms.[2] Recently, more environmentally friendly anti-fouling coatings have become a focus in research.[2-8] The new coatings are usually designed to satisfy one of two requirements: anti-fouling (reduce or minimize biofouling that occurs) or fouling-release (biofouling does occur, but the foulants can be easily released from the coating surface). Anti-fouling and fouling-release performance of a coating is determined by both the surface properties (e.g., surface chemical, topographic, and biological features) and bulk properties (e.g., Young's modulus) of the coating.

In order to fully characterize and better develop marine anti-fouling and fouling release coatings, an understanding of the surface features of the coating is needed. Extensive research has been performed to achieve in-depth understanding of surface biological and topographical characteristics in aqueous environments using various methods such as marine field tests,[9] lab biological assays,[10] and AFM.[11] Determining chemical information about the coating is more challenging. Most surface sensitive approaches have disadvantages when examining surface chemical information in aqueous environments. For example, regular X-ray photoelectron spectroscopy (XPS) and near edge X-ray absorption fine structure (NEXAFS) spectroscopy require an ultra high vacuum environment and thus cannot be applied to study surfaces in water. It is also difficult to directly relate such a surface structure probed in vacuum to the anti-fouling and fouling-release behaviors of such a material, because it is believed that such behaviors are mediated by the surface structure of the material in an aqueous environment, which is very likely different from that in vacuum. Regular XPS is unable to characterize whether the hydrophobic segments are still present at the surface when the polymer film is placed in an aqueous environment. Freeze-drying XPS may detect surface chemical compositions of surfaces, but the sample preparation procedure is complicated and no orientation information of surface functional groups can be deduced.[12] Contact angle measurements can be used to study surface hydrophobicity, but no chemical information can be obtained. Attenuated total reflection infrared spectroscopy (ATR-FTIR) can be applied to study solid/liquid interfaces.[13] However, the surface sensitivity of ATR-FTIR is limited, and the signals may suffer from water absorption bands that can obscure vital information. In this work, sum frequency generation (SFG) is applied to investigate surface structures of several polymers developed recently as marine coatings.

1.2 SUM FREQUENCY GENERATION VIBRATIONAL SPECTROSCOPY

SFG is a nonlinear optical technique that has recently proven to be useful in probing surfaces and interfaces. As an optical technique it has numerous advantages. It can probe any surface or interface where light is accessible. It is also nondestructive, highly sensitive, and has good spatial, temporal, and spectral properties. SFG is useful to probe surfaces and interfaces through collecting vibrational spectra of surfaces and interfaces. The peak centers and peak intensities in the SFG spectra are related to the type, coverage, orientation, and orientation distribution of the functional groups present at the surface.[14-26] This allows SFG to not only determine what is at the surface, but also provides an idea of how well ordered the surface is. There has been much work using SFG on polymer surface in both air and water,[27-36] as well as on biological systems including proteins, peptides, and model cell membranes.[37-43]

1.2.1 Basic SFG Theory

The polarization (the dipole moment per unit volume), *P*, of a molecule present in an electric field can be written as follows:[16]

$$P = \varepsilon_0(\chi^{(1)}E + \chi^{(2)} : EE + \chi^{(3)} \vdots EEE + ...) \qquad (1.1)$$

Where ε_0 is the dielectric constant, $\chi^{(1)}$ is the linear susceptibility, and $\chi^{(2)}$, $\chi^{(3)}$, and higher terms are nonlinear susceptibilities of the second-order, third-order, etc. For weak electric fields, higher order terms are small and so they can be ignored, therefore the polarization is directly proportional to the linear susceptibility, such as the case in Raman spectroscopy. When the electric fields are strong, polarization is also dependent on higher terms that result from multiple electric fields. The higher order terms are thus deemed to have nonlinear response from the sample. The second order nonlinear susceptibility $\chi^{(2)}$ governs such processes as second harmonic generation (SHG), SFG, and difference frequency generation (DFG). The third order nonlinear susceptibility $\chi^{(3)}$ is for processes involving four wave mixing such as coherent anti-stokes Raman spectroscopy (CARS).

This work focuses on $\chi^{(2)}$, as this is the term which SFG is dependent on. For SFG, $\chi^{(2)}$ is associated with the signal generated by two strong electric fields, e.g., input beams at ω_1 and ω_2. The polarization arising from $\chi^{(2)}$ can be expressed as follows:[16]

$$P^{(2)} = \varepsilon_0 \chi^{(2)} : E_1 E_2 \cos(\omega_1 t)\cos(\omega_2 t) \tag{1.2}$$

Using basic trigonometric relationships this can be rearranged:[16]

$$P^{(2)} = \frac{1}{2}\varepsilon_0 \chi^{(2)} : E_1 E_2 [\cos(\omega_1 + \omega_2)t + \cos(\omega_1 - \omega_2)t] \tag{1.3}$$

It can be seen that the induced dipoles generated by the two input beams oscillate at both $(\omega_1 + \omega_2)$ and $(\omega_1 - \omega_2)$. The first term corresponds to the SFG process and the second is the DFG process. All the SFG research present in this work utilizes an SFG experimental setup with a frequency fixed visible beam, ω_1, and a frequency tunable infrared beam, ω_2. As ω_2 is scanned over a range of frequencies, when it matches a vibrational transition, the SFG signal becomes resonantly enhanced, producing a vibrational spectrum.

As the beams used to generate the SFG signal are coherent laser beams the generated SFG signal is also coherent. The basic process of SFG and a simple schematic of the experimental setup are shown in Figure 1.1. The surface sensitivity of SFG arises from the nonlinear susceptibility, $\chi^{(2)}$. As $\chi^{(2)}$ is a third-rank polar tensor, upon inversion: $\chi^{(2)}(r) = -\chi^{(2)}(-r)$. However for materials with an inversion center: $\chi^{(2)}(r) = \chi^{(2)}(-r)$. The only time at which both relationships hold true is when $\chi^{(2)}(-r) = -\chi^{(2)}(-r) = 0$. This relationship results in no SFG signal being generated for materials with an inversion center. As most bulk materials have an inversion center, SFG cannot be generated from these bulk materials. SFG can be only generated where the inversion symmetry is broken. This occurs at surfaces and interfaces, allowing for SFG to be specifically

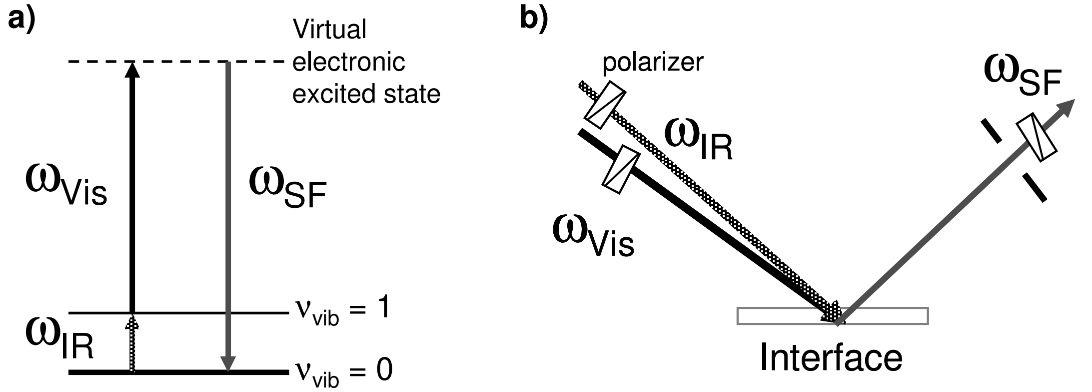

Figure 1.1. Schematics of (a) the SFG process with the IR photon matching a vibrational transition, and the visible photon exciting the molecule to a virtual electronic excited state, and (b) the general experimental setup of an SFG measurement with polarizers to control the input and detected beams polarization.

surface/interface sensitive. Combining the surface specificity of SFG with various polarization combinations of input and output beams enables SFG to determine orientation information of surface groups.[44-49]

1.2.2 Orientation Analysis by SFG

The intensity of the SFG signal in the reflected direction can be expressed as follows:[20]

$$I(\omega) = \frac{8\pi^3\omega^3 \sec^2 \beta}{c^3 n(\omega) n(\omega_1) n(\omega_2)} \left|\chi_{eff}^{(2)}\right|^2 I_1(\omega_1) I_2(\omega_2) \qquad (1.4)$$

Where $n(\omega)$ is the refractive index of the medium at the frequency ω, β is the angle of reflection of the generated SFG beam, $I(\omega)$ is the intensity of the input beam at frequency ω, $\chi_{eff}^{(2)}$ is the effective second order nonlinear susceptibility tensor, which can be related to the second order nonlinear susceptibility tensor defined in the lab coordinate system, $\chi^{(2)}$. $\chi^{(2)}$ is a third-rank tensor with 27 components, however only 7 of them are nonzero for nonchiral materials with azimuthal symmetry: $\chi_{yyz}^{(2)} = \chi_{xxz}^{(2)}$, $\chi_{yzy}^{(2)} = \chi_{xzx}^{(2)}$,

$\chi^{(2)}_{zyy} = \chi^{(2)}_{zxx}$, and $\chi^{(2)}_{zzz}$. Through the use of polarizers and mirrors the polarization of all three beams can be controlled. This results in the ability to probe only one component of $\chi^{(2)}$ at a time.[20,50] The relationship between $\chi^{(2)}_{eff}$ and $\chi^{(2)}$ can be seen below:

$$\chi^{(2)}_{eff,ssp} = L_{yy}(\omega)L_{yy}(\omega_1)L_{zz}(\omega_2)\sin\beta_2\chi^{(2)}_{yyz}$$

$$\chi^{(2)}_{eff,sps} = L_{yy}(\omega)L_{zz}(\omega_1)L_{yy}(\omega_2)\sin\beta_1\chi^{(2)}_{yzy}$$

$$\chi^{(2)}_{eff,pss} = L_{zz}(\omega)L_{yy}(\omega_1)L_{yy}(\omega_2)\sin\beta\chi^{(2)}_{zyy} \tag{1.5}$$

$$\begin{aligned}\chi^{(2)}_{eff,ppp} = &-L_{xx}(\omega)L_{xx}(\omega_1)L_{zz}(\omega_2)\cos\beta\cos\beta_1\sin\beta_2\chi^{(2)}_{xxz}\\ &-L_{xx}(\omega)L_{zz}(\omega_1)L_{xx}(\omega_2)\cos\beta\sin\beta_1\cos\beta_2\chi^{(2)}_{xzx}\\ &+L_{zz}(\omega)L_{xx}(\omega_1)L_{xx}(\omega_2)\sin\beta\cos\beta_1\cos\beta_2\chi^{(2)}_{zxx}\\ &+L_{zz}(\omega)L_{zz}(\omega_1)L_{zz}(\omega_2)\sin\beta\sin\beta_1\sin\beta_2\chi^{(2)}_{zzz}\end{aligned}$$

Where $L_{ii}(\omega)$ is the Fresnel coefficient for the beam at frequency ω, and β_1 and β_2 are the angles of reflection for the input visible and IR beams.

By fitting the collected SFG spectrum, $\chi^{(2)}_{eff}$ component for a given polarization combination and vibrational mode can be determined. The intensity of the collected SFG signal can be estimated by:[48]

$$I_{ijk}(\omega) \propto \left|\chi_{ijk,nr} + \sum_q \frac{A_{ijk,q}}{\omega - \omega_q + i\Gamma_q}\right|^2 \tag{1.6}$$

Where I_{ijk} is the intensity for signal collected with a given polarization combination, $\chi_{ijk,NR}$ is the nonresonant background contribution, ω is the IR wavelength, $A_{ijk,q}$, ω_q, and Γ_q are the strength, resonant frequency, and damping coefficient of the vibrational mode q, respectively.

Orientation of surface functional groups can be obtained through SFG signals detected with different polarization combinations and/or signals from different vibrational modes in an SFG spectrum. While only Chapter 5 will deal extensively with orientation analysis, it is still important to understand the principles. Here using a mono-substituted phenyl group, the process of determining orientation information from SFG spectra will be introduced. As stated previously, different components of $\chi^{(2)}$ can be explored by different polarization combinations. $\chi^{(2)}$ (in the lab coordinate system) is related to the molecular hyperpolarizability $\beta^{(2)}$ (in the molecular frame) by the orientation angles, θ, of the phenyl group (or other functional groups).[21,25,26,48,51] With a knowledge of the $\beta^{(2)}$, the assorted measured components of $\chi^{(2)}$ can be used to determine the orientation.[48] Assuming isotropic twist around the c-axis of the functional group, as well as knowing a symmetry group, such as C_{2v} for phenyl groups, and a δ distribution, a relationship between $\chi^{(2)}$ and $\beta^{(2)}$ can be developed. For a mono-substituted phenyl group the following relationships for the ν_2 mode (Figure 1.2) can be found:[26,27,29]

$$\chi_{yyz,\upsilon 2} = N_s\beta_{ccc}\left(\frac{\mathrm{Cos}[\theta]-\mathrm{Cos}[3\theta]}{8} + \frac{7\mathrm{Cos}[\theta]+\mathrm{Cos}[3\theta]}{16}r\right) \quad (1.7)$$

$$\chi_{yzy,\upsilon 2} = N_s\beta_{ccc}\left(\frac{\mathrm{Cos}[\theta]-\mathrm{Cos}[3\theta]}{8} - \frac{\mathrm{Cos}[\theta]-\mathrm{Cos}[3\theta]}{16}r\right) \quad (1.8)$$

Where r is the ratio of β_{ccc} to β_{aac} and is a known value. In this case r is ~1. It can be seen in the equations that there is also a dependence of $\chi^{(2)}$ components on the number density, N_s, of the functional group, resulting in both N_s and θ being unknown. Using a ratio of two different $\chi^{(2)}$ components simplifies the process as the N_s drops out of the ratio.[29,48]

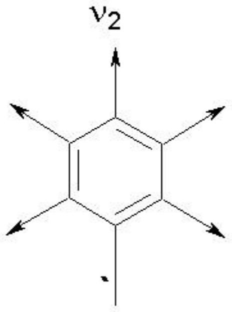

Figure 1.2. Schematic of the ν_2 mode for a mono-substituted phenyl ring.

$$\frac{\chi_{yyz,\nu 2}}{\chi_{yzy,\nu 2}} = \frac{\frac{\mathrm{Cos}[\theta]-\mathrm{Cos}[3\theta]}{8}+\frac{7\mathrm{Cos}[\theta]+\mathrm{Cos}[3\theta]}{16}r}{\frac{\mathrm{Cos}[\theta]-\mathrm{Cos}[3\theta]}{8}-\frac{\mathrm{Cos}[\theta]-\mathrm{Cos}[3\theta]}{16}r} \tag{1.9}$$

However the assumption of a δ distribution for orientation angles is not always accurate. To allow for a broader range of angles a Gaussian function is included using the average of the tilt angles. This can be shown in the following equations:[29]

$$<\cos^n\theta>=\int_0^{\pi}\cos^n\theta f(\theta)\sin\theta d\theta \tag{1.10}$$

$$f(\theta)=C\exp[-(\theta-\theta_0)^2/2\sigma^2] \tag{1.11}$$

Where the < > implies the averaging, f(θ) is the Gaussian function, *C* is a normalization constant, θ_0 is related to the average orientation angle of the group versus the surface normal and σ is the angle distribution parameter. In this case it is necessary to determine both the θ_0 and σ to understand the orientation distribution of the functional group.

1.2.3 SFG Instrumentation

SFG spectra were collected using an EKSPLA system. The system consists of four components, shown in Figure 1.3: a pico-second Nd:YAG laser operating at a repetition rate of 20Hz; a harmonics unit containing two KD*P; an optical parametric

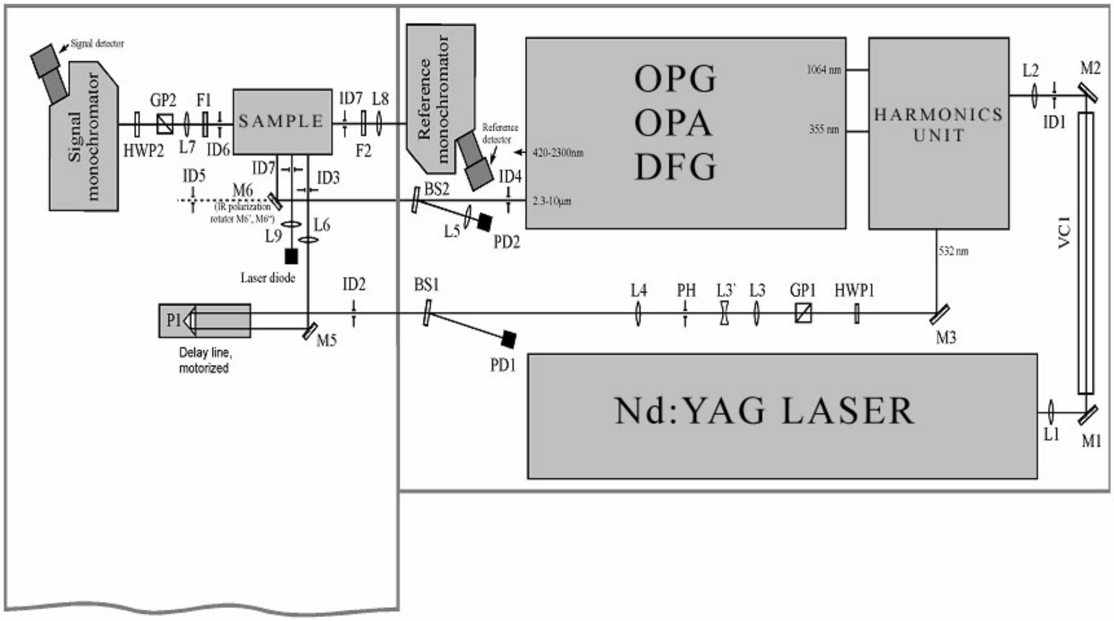

Figure 1.3. Layout of the EKSPLA SFG system used in this research.

generation/optical parametric amplification/difference frequency generation unit (OPG/OPA/DFG) utilizing a LBO crystal for the OPG/OPA portion and $GaAgS_2$ crystal for the DFG; and lastly the sample stage and detection system. The Nd:YAG laser generates a fundamental output at 1064 nm with pulses that have a 20 ps pulse width. The fundamental is then sent to the harmonics unit where a portion of it undergoes SHG to produce a 532 nm beam. Part of the 532 nm beam is sent through a delay line and on to the sample stage. The remaining 532 nm beam passes through the second KD*P crystal to become the third harmonic of the fundamental at 355 nm, which is sent with the remaining fundamental to the OPG/OPA/DFG unit. The OPG/OPA is fed from the 355 nm to generate a frequency tunable visible signal and frequency tunable near IR infrared idler beam. The signal beam is blocked by a filter. The idler meets with the fundamental in the $GaAgS_2$ crystal to undergo DFG to generate the frequency tunable mid-IR beam.

The mid-IR beam can be tuned from 1000-4000 cm^{-1} with varying energies depending on the frequency. For the C-H stretching region (2800-3100 cm^{-1}) the IR energy is ~160 μJ; while in the C-F (~1300 cm^{-1}) stretching region it is ~40 μJ. The visible energies are adjusted depending on the sample geometry used (Figure 1.4). For both window geometries, face-down and face-up, the visible energy used was ~150 μJ unless otherwise specified. In the total internal reflection (TIR) prism geometry the energy was reduced to ~40 μJ.

The input beams at the sample stage have angles of 60° for the visible and 54° for the IR with respect to the surface normal. The spot size for both beams is ~500 μm in diameter. The reflected signal is then collected and sent to a gated photomultiplier through a monochromator to separate the much stronger 532 nm visible from the weaker blue shifted SFG signal. The powers of the fixed visible and tunable IR beams are collected by using the back reflection from beam splitters, placed for this purpose, into two photodiodes. These values are then used to normalize for fluctuations in the laser during the acquisition of spectra. The various polarization combinations are achieved by using Gland prism polarizers for the input visible and SFG signal beams and combinations of mirrors for the tunable IR. The polarization combinations presented in this work consist of ssp (s-polarized SFG, s-polarized visible input, and p-polarized IR input), ppp, and sps.

As shown in Figure 1.4, three different geometries were used to collect data. The majority of work done using windows was collected in the face-down geometry. This allowed for easy collection of polymer/air interface signals, as the signals are reflected back and the IR and visible beams pass primarily through the sample. However, due to

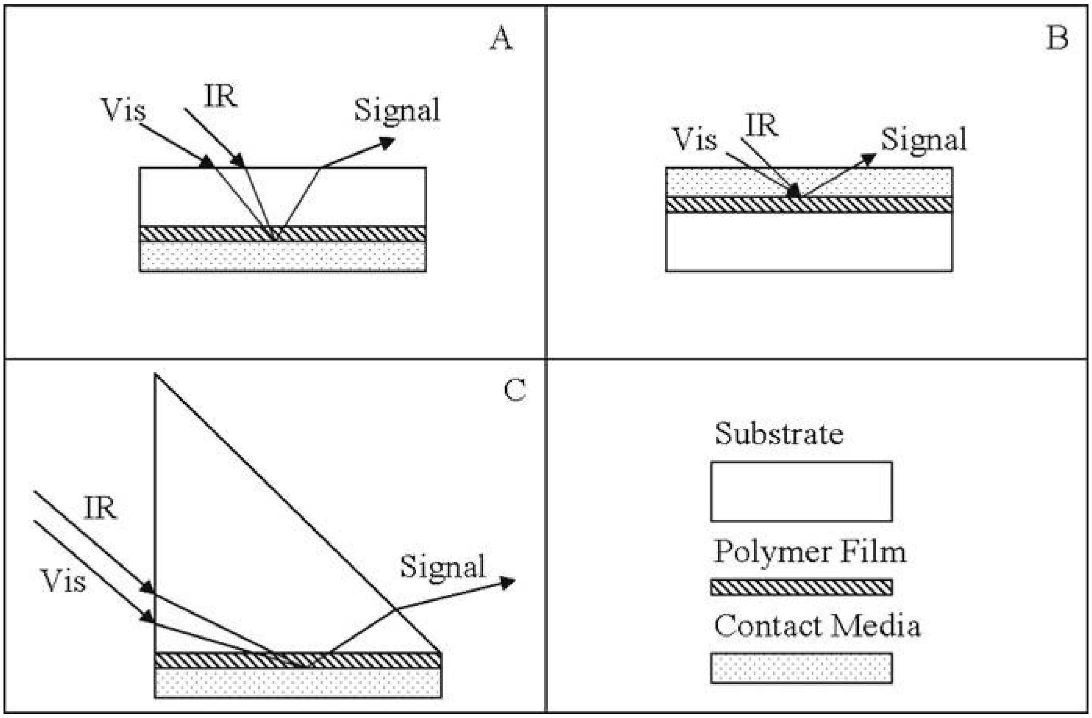

Figure 1.4. Three different geometries used in SFG. (A) Face-down window: Visible and infrared beams go through substrate and bulk polymer to polymer/media interface to generate signal beam. (B) Face-up window: Visible and infrared beams mix at media/polymer interface to generate signal beam. (C) Total internal reflection prism: Visible and infrared beams pass through leg of prism and polymer thin film to overlap at the polymer/media interface and generate signal beam.

the absorption of the IR at lower wavenumbers by the substrate, a face-up geometry was adopted to collect spectra in the C-F stretching region. In this geometry, the SFG is collected in the same way as face-down, but due to the re-orientation the collected signals are weaker in intensity compared to their corresponding face-down counter parts. The TIR prism geometry used results in much stronger signals even with weaker pump energies. This allows for the detection of signals that may not have been observed in the face-down geometry.[52]

1.3 PRESENTED RESEARCH

The goal of this work is to investigate the surface behavior of polymers intended for use as anti-fouling coatings. A wide variety of materials have been investigated as anti-fouling materials including: polyethylene glycol, polydimethylsiloxane, zwitterionic based materials, amphiphilic based materials, and materials with biocides incorporated into the structure. Specifically, this work will deal with amphiphilic based polymers and materials with a cationic biocide incorporated in. Examples of these materials can be seen in Figure 1.5.[53,54] This research will be divided into several components. Half of the work will be focused on polymer surface restructuring after the material has been contacted with a new medium, such as air or water. An investigation of the peak assignment of a vibrational mode seen in the C-F stretching will also be discussed as several of the polymers under study contain fluorinated portions. Lastly orientation analysis for para-substituted phenyl groups has been developed.

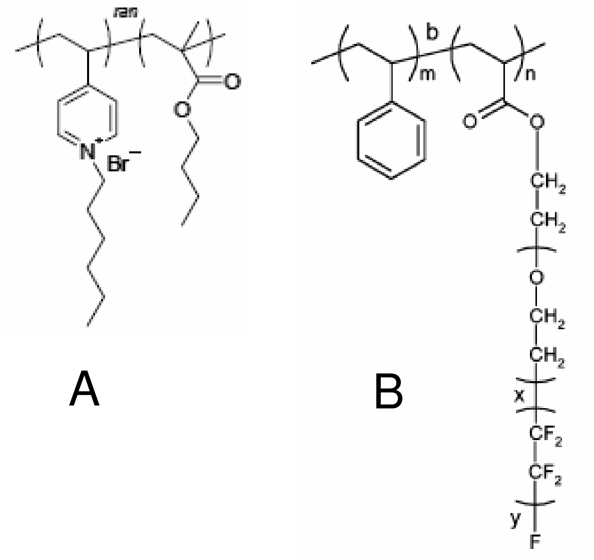

Figure 1.5. Structures of a di-block polymer with a pyridinium biocide in cooperated (A) and an amphiphilic polymer with a ethylene glycol and fluoroalkyl side-chain (B).

In Chapter 2 a discussion of the surface properties of cationic di-block copolymers containing pyridinium functionality will be examined by SFG. The interaction between the cationic polymers and a lipid bilayer, acting as a model for bacterial cell membrane, was investigated. The presence of a fluorinated segment in the copolymer has significant effect on the time dependent disruption of the lipid bilayer. To fully understand this behavior, spectra were initially collected at the polymer/air and polymer/water interface using face-down window geometry. However, as no signal was observed at the polymer/water interface, a TIR prism geometry was adopted to increase the SFG signal. Upon collection of these signals it became apparent that the prism geometry generated additional signals besides the polymer/air or polymer/water signal. These signals could arise from the buried substrate/polymer interface or even be bulk signals.

Since a new amphiphilic tri-block copolymer was developed for anti-fouling purpose, it was decided to further explore the origin of the SFG signals from the buried polymer/substrate interface using the new copolymer. Such results will be discussed in Chapter 3. By varying the thickness of the polymer thin film, significantly different intensity of the SFG signals could be observed. As the film thickness increased, the collected SFG signals decreased. Calculations of the Fresnel coefficients showed that the polymer/air interface signal should remain near constant and that the substrate/polymer signal should actually increase when the film thickness increases. Further analysis showed that the SFG signal is mostly from the polymer/air interface, but as the thickness increases the buried interface signal increases and destructively interferes with the polymer/air signals. The process was then repeated on the polymer/water interface and similar results were seen. As a portion of the polymer was fluorinated, SFG spectra were also collected in the C-F stretching region. It was observed that the fluorinated portions were present at the surface in both the air and water environments. While expected in the case of the air, the presence of the highly hydrophobic fluorinated groups in water was unexpected.

The peak assignment of the observed C-F stretch modes has some controversy, which are further studied in Chapter 4. In order to better understand the C-F stretching assignment, a simpler system was investigated. Self-assembled thin layer formed by a fluorinated trichlorosilane was examined. Further characterization revealed that the samples prepared were not ideal monolayers. Even so, using SFG and a variety of other analytical tools, the structures of these thin films of different sample preparation conditions, were successfully characterized.

The last portion of this work centers on the development of a data analysis method to deduce para-substituted phenyl group orientation. Previous work has been done to understand mono-substituted phenyl groups, however, several of the anti-fouling copolymers investigated in this work included para-substituted phenyl groups. No strong phenyl signals were observed for the copolymers; therefore a sulfonated polystyrene which generates strong phenyl SFG signals was studied. In the case of a mono-substituted phenyl, the SFG data can be interpreted by assuming that the twist angle of the molecule is isotropic, thus only the tilt angle need be considered. It was found for para-substituted phenyl groups that both the tilt and twist angles need to be considered.

1.4 REFERENCES

(1) Schultz, M. P. *Biofouling* **2007**, *23*, 331-341.

(2) Yebra, D. M.; Kiil, S.; Dam-Johansen, K. *Prog. Org. Coat.* **2004,** *50*, 75-104.

(3) Krishnan, S.; Weinman, C. J.; Ober, C. K. *J. Mater. Chem.* **2008**, *18*, 3405-3413.

(4) Genzer, J.; Efimenko, K. *Biofouling* **2006**, *22*, 339-360.

(5) Webster, D. C.; Chisholm, B. J.; Stafslien, S. J. *Biofouling* **2007**, *23*, 179-192.

(6) Joshi, R. G.; Goel, A.; Mannari, V. M.; Finlay, J. A.; Callow, M. E.; Callow, J. A. *J. App.l Polym. Sci.* **2009**, *114*, 3693-3703.

(7) Chambers, L.D.; Stokes, K. R.; Walsh, F. C.; Wood, R. J. K. *Surf. Coat. Technol.* **2006**, *201*, 3642–3652.

(8) Chen. S.; Jiang, S.; *Adv. Mater.* **2008**, *20*, 335-338.

(9) Swain, G. W.; Anil, A. C.; Baier, R. E.; Chia, F.; Conte, E.; Cook, A.; Hadfield, M.; Haslbeck, E.; Holm, E.; Kavanagh, C.; Kohrs, D.; Kovach, B.; Lee, C.; Mazzella, L.; Meyer, A. E.; Qian, P.; Sawant, S. S.; Schultz, M.; Sigurdsson, J.; Smith, C.; Soo, L.; Terlizzi, A.; Wagh, A.; Zimmerman, R.; Zupo, V. *Biofouling* **2000,** *16*, 331-344.

(10) Finlay, J. A.; Krishnan, S.; Callow, M. E.; Callow, J. A.; Dong, R.; Asgill, N.; Wong, K.; Kramer, E. J.; Ober, C. K.; *Langmuir* **2008**, *24*, 503-510.

(11) Bartels, J. W.; Cheng, C.; Powell, K. T.; Xu, J.; Wooley, K. L. *Macromol. Chem. Phys*. **2007**, *208*, 1676-1687.

(12) Anderson, E. M; Noble, M. L.; Garty, S.; Ma, H.; Bryers, J. D.; Shen, T. T.; Ratner, B. D. *Biomaterials*, **2009**, *30*, 5675-5681.

(13) Wang, J.; Paszti, Z.; Clarke, M. L.; Chen, X.; Chen, Z. *J. Phys. Chem. B* **2007**, *111* 6088–6095.

(14) Shen, Y. R. *The Principles of Nonlinear Optics;* John Wiley & Sons: New York, 1984.

(15) Shen, Y. R. *Annu. Rev. Phys. Chem.* **1989***, 40*, 327-350.

(16) Bain, C. D. *J. Chem. Soc. , Faraday Trans.* **1995***, 91*, 1281-1296.

(17) Eisenthal, K. B. *Chem. Rev.* **1996***, 96*, 1343-1360.

(18) Löbau, J.; Wolfrum, K. *J. Opt. Soc. Am. B* **1997***, 14*, 2505-2512.

(19) Walker, R. A.; Gruetzmacher, J. A.; Richmond, G. L. *J. Am. Chem. Soc.* **1998***, 120*, 6991-7003.

(20) Miranda, P. B.; Shen, Y. R. *J. Phys. Chem. B* **1999***, 103*, 3292-3307.

(21) Gracias, D. H.; Chen, Z.; Shen, Y. R.; Somorjai, G. A. *Acc. Chem. Res.* **1999***, 32*, 930-940.

(22) Pizzolatto, R. L.; Yang, Y. J.; Wolf, L. K.; Messmer, M. C. *Anal. Chim. Acta* **1999***, 397*, 81-92.

(23) Shultz, M. J.; Schnitzer, C.; Simonelli, D.; Baldelli, S. *Int. Rev. Phys. Chem.* **2000***, 19*, 123-153.

(24) Kim, J.; Cremer, P. S. *J. Am. Chem. Soc.* **2000***, 122*, 12371-12372.

(25) Gautam, K. S.; Schwab, A. D.; Dhinojwala, A.; Zhang, D.; Dougal, S. M.; Yeganeh, M. S. *Phys. Rev. Lett.* **2000***, 85*, 3854-3857.

(26) Briggman, K. A.; Stephenson, J. C.; Wallace, W. E.; Richter, L. J. *J. Phys. Chem. B* **2001***, 105*, 2785-2791.

(27) Wang, J.; Woodcock, S. E.; Buck, S. M.; Chen, C.; Chen, Z. *J. Am. Chem. Soc.* **2001***, 123*, 9470-9471.

(28) Chen, Z.; Shen, Y. R.; Somorjai, G. A. *Annu. Rev. Phys. Chem.* **2002***, 53*, 437-465.

(29) Chen, C.; Wang, J.; Woodcock, S. E.; Chen, Z. *Langmuir* **2002***, 18*, 1302-1309.

(30) Wilson, P. T.; Briggman, K. A.; Wallace, W. E.; Stephenson, J. C.; Richter, L. J. *Appl. Phys. Lett.* **2002***, 80*, 3084-3086.

(31) Liu, Y.; Messmer, M. C. *J. Phys. Chem. B* **2003***, 107*, 9774-9779.

(32) Hong, S.; Zhang, C.; Shen, Y. R. *Appl. Phys. Lett.* **2003***, 82*, 3068-3070.

(33) Rao, A.; Rangwalla, H.; Varshney, V.; Dhinojwala, A. *Langmuir* **2004***, 20*, 7183-7188.

(34) McGall, S. J.; Davies, P. B.; Neivandt, D. J. *J. Phys. Chem. B* **2004***, 108*, 16030-16039.

(35) Sung, J.; Kim, D.; Whang, C. N.; Ohe, M.; Yokoyama, H. *J. Phys. Chem. B* **2004***, 108*, 10991-10996.

(36) Li, G.; Ye, S.; Morita, S.; Nishida, T.; Osawa, M. *J. Am. Chem. Soc.* **2004***, 126*, 12198-12199.

(37) Wang, J.; Buck, S. M.; Chen, Z. *J. Phys. Chem. B* **2002***, 106*, 11666-11672.

(38) Wang, J.; Buck, S. M.; Even, M. A.; Chen, Z. *J. Am. Chem. Soc.* **2002***, 124*, 13302-13305.

(39) Jung, S.; Lim, S.; Albertorio, F.; Kim, G.; Gurau, M. C.; Yang, R. D.; Holden, M. A.; Cremer, P. S. *J. Am. Chem. Soc.* **2003***, 125*, 12782-12786.

(40) Kim, J.; Somorjai, G. A. *J. Am. Chem. Soc.* **2003***, 125*, 3150-3158.

(41) Dreesen, L.; Humbert, C.; Sartenaer, Y.; Caudano, Y.; Volcke, C.; Mani, A. A.; Peremans, A.; Thiry, P. A.; Hanique, S.; Frere, J. *Langmuir* **2004***, 20*, 7201-7207.

(42) Doyle, A. W.; Fick, J.; Himmelhaus, M.; Eck, W.; Graziani, I.; Prudovsky, I.; Grunze, M.; Maciag, T.; Neivandt, D. J. *Langmuir* **2004***, 20*, 8961-8965.

(43) Chen, X.; Clarke, M. L.; Wang, J.; Chen, Z. *Int. J. Mod. Phys. B* **2005***, 19*, 691-713.

(44) Guyot-Sionnest, P.; Hunt, J. H.; Shen, Y. R. *Phys. Rev. Lett.* **1987***, 59*, 1597-1600.

(45) Hirose, C.; Akamatsu, N.; Domen, K. *J. Chem. Phys.* **1992***, 96*, 997-1004.

(46) Hirose, C.; Akamatsu, N.; Domen, K. *Appl. Spectrosc.* **1992***, 46*, 1051-1071.

(47) Hirose, C.; Yamamoto, H.; Akamatsu, N.; Domen, K. *J. Phys. Chem.* **1993***, 97*, 10064-10069.

(48) Zhuang, X.; Miranda, P. B.; Kim, D.; Shen, Y. R. *Physical Review B: Condensed Matter and Materials Physics* **1999***, 59*, 12632-12640.

(49) Wang, J.; Paszti, Z.; Even, M. A.; Chen, Z. *J. Am. Chem. Soc.* **2002***, 124*, 7016-7023.

(50) Wang, J.; Chen, C.; Buck, S. M.; Chen, Z. *J. Phys. Chem. B* **2001***, 105*, 12118-12125.

(51) Wei, X.; Zhuang, X.; Hong, S.; Goto, T.; Shen, Y. R. *Phys. Rev. Lett.* **1999***, 82*, 4256-4259.

(52) Wang, J.; Even, M. A.; Chen, X.; Schmaier, A. H.; Waite, J. H.; Chen, Z. *J. Am. Chem. Soc.* **2003***, 125*, 9914-9915.

(53) Krishnan, S.; Ayothi, R.; Hexemer, A.; Finlay, J. A.; Sohn, K. E.; Perry, R.; Ober, C. K.; Kramer, E. J.; Callow, M. E.; Callow, J. A.; Fischer, D. A. *Langmuir* **2006**, *22*, 5975-5086.

(54) Krishnan, S.; Ward, R. J.; Hexemer, A.; Sohn, K. E.; Lee, K. L.; Angert E. R.; Fischer D. A.; Kramer, E. J.; Ober, C. K. *Langmuir* **2006**, *22*, 11255-11266.

CHAPTER 2: SURFACE STUDIES OF ANTI-FOULING CATIONIC BLOCK COPOLYMERS BY SUM FREQUENCY GENERATION SPECTROSCOPY

2.1 INTRODUCTION

One method to develop anti-fouling coatings is through the use of cationic polymers. Cationic polymers have proven to be useful as antimicrobial materials.[1] It is thought that the electrostatic interaction between the positively charged polymer and the negatively charged bacterial cell membrane results in the antimicrobial activity of the polymer. The exact mechanism for the antimicrobial behavior of cationic polymers is not yet understood. One mechanism under study is the insertion of hydrophobic alkyl groups into the cell membrane, resulting in the membrane disruption.[2] Another proposed mechanism is due to the charge density of the polymer which leads to the release of cations from the cell membrane. The removal of the cations is thought to cause destabilization of the membrane which ruins the efficacy of the membrane and results in cell death.[3]

One such moiety used in cationic polymers is pyridinium. *N*-hexylpyridinium was shown to be an effective antimicrobial material even in the absence of a liquid media when used as a surface-tethered brush.[4] Different lengths of *n*-alkyl bromides used in the *N*-alkylation of the pyridine rings had varying results on the antimicrobial activity against *S. aureus*. It was also found that the molecular weight of the base polymer poly(4-vinylpyridine) (P4VP) was important for antimicrobial properties. Polymers **1 (B)**, **2 (H)**,

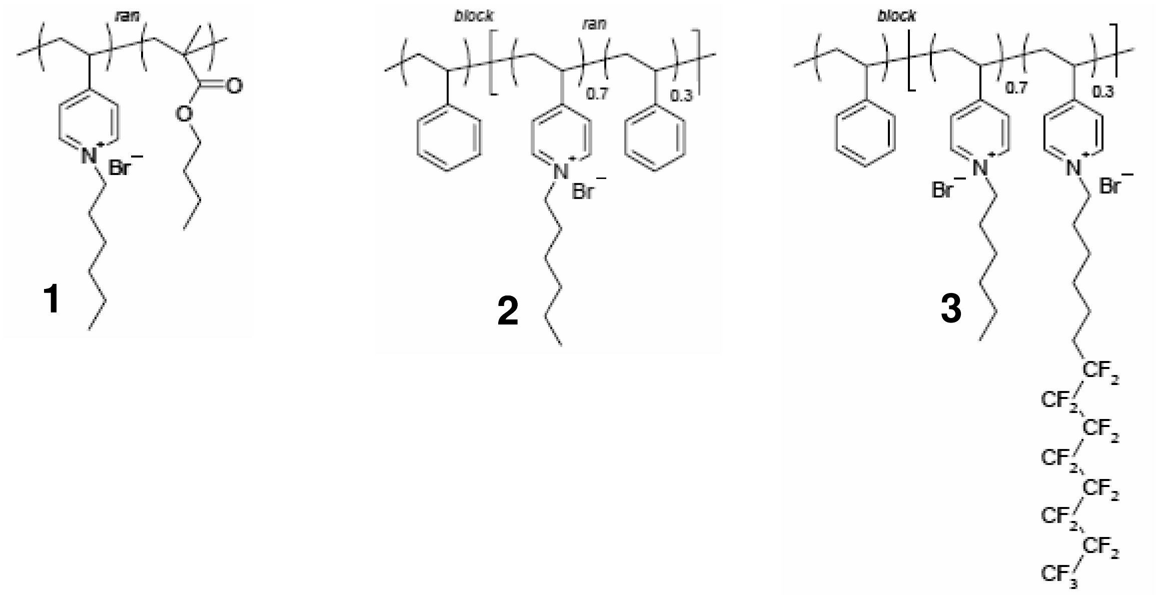

Figure 2.1. Structures of polymers **1**, **2**, and **3**.

and **3 (E)** (Figure 2.1) were developed at Cornell University in the Christopher Ober group for use as anti-fouling coatings based on these findings. In their research, they found that the density of the pyridinium rings at the surface and the length of the pyridinium chains had an effect on the antimicrobial properties of the polymer.[5]

Previous research on antimicrobial peptides (Melittin) and their synthetic mimics (T5) with SFG has focused on their interactions with lipid bilayers.[6,7] In those studies, model bacterial membranes were prepared by use of pure lipid bilayers. Then a solution of Melittin or T5 was introduced to contact the lipid bilayer and the resulting interaction at the lipid bilayer surface was observed. In the case of the synthetic mimic, T5, the adsorption of the molecules to the bilayer was observed along with the eventual insertion and reorientation of the molecule in the lipid bilayer.

Understanding how polymers **1**, **2**, and **3** interact with a lipid bilayer through SFG studies would allow for the better development of future materials that could be tailored to address the specific interactions between antimicrobial materials and bacterial cell membranes. Also, understanding the surface behavior of the polymers in an aqueous environment would provide further insight into the surface structures of these coatings, and the interaction mechanisms involved between the polymers and bacterial cell membranes. Due to the insoluble nature of the polymers in water, a slightly different approach was taken to study polymer-lipid bilayer interactions. Here, by mixing the lipid and polymer together, the interaction between the model membrane and polymer could be seen in a similar fashion to that observed for Melittin or T5, which will be discussed in detail below.

2.2 EXPERIMENTAL

2.2.1 Reagents

Deuterium oxide (D_2O), *N,N*-dimethylformamide (DMF), and chloroform were purchased from Sigma-Aldritch (St. Louis, MO) and used as is. Hydrogenated 1,2-dipalmitoyl-*sn*-glycerol-3-phosphoglycerol (DPPG) and deuterated 1,2-dipalmitoyl-*sn*--glycerol-3-phosphoglycerol (dDPPG) were purchased from Avanti Polar Lipids (Alabaster, AL) and diluted to 1 mg/mL solutions in chloroform for future use. Calcium fluoride (CaF_2) right angle prisms were obtained from Altos Photonics (Bozeman, MT). One inch diameter, 1/8 inch thick IR grade fused silica windows were ordered from Esco Products (Oakridge, NJ).

2.2.2 Sample Preparation

A monolayer of dDPPG was prepared on the leg side of a CaF_2 prism by Langmuir-Blodgett method. A mixed solution of DPPG and 1% wt/wt of polymer **1**, **2**, or

3 were made in chloroform. The dDPPG coated prism was mounted so that one leg side of the prism was perpendicular to the water surface. The prism was lowered onto a monolayer of the mixed DPPG/polymer prepared at the SFG samples stage to form a dDPPG-DPPG/polymer bilayer. SFG signal was collected from this bilayer (incorporated) with polymer as a function of time.

For polymer surface studies, polymers **1**, **2**, and **3** were made into 2% wt/wt solutions in DMF. Fused silica windows and CaF_2 were then coated with polymer solutions by spin-casting at 2500 rpms. SFG spectra were collected from these polymer surfaces in air and in water.

2.2.3 Instrumentation

SFG spectra were collected using the instrument described in Chapter 1 using both the face-down window geometry and the TIR prism geometry. Spectra were obtained in ssp (s-polarized SFG output, s-polarized visible input, and p-polarized IR input), ppp and sps polarization combinations. Each spectrum presented here is the average of at least 3 independent measurements. Deuterated DPPG monolayer was prepared on a KSV Langmuir-Blodgett trough (Linthicum Heights, MD).

2.3 RESULTS AND DISCUSSION

2.3.1 Lipid Bilayer-Polymer Interaction

Time dependent ssp SFG signals of both the CH_3 symmetric stretch found at ~2880 cm^{-1} and the CD_3 symmetric stretch at ~2070 cm^{-1} were collected from the lipid bilayers with 1% wt/wt polymers **1**, **2**, or **3** present in the outer leaflet. Figure 2.2 displays such time dependent SFG signals for polymers **1**, **2**, and **3**, respectively. Both

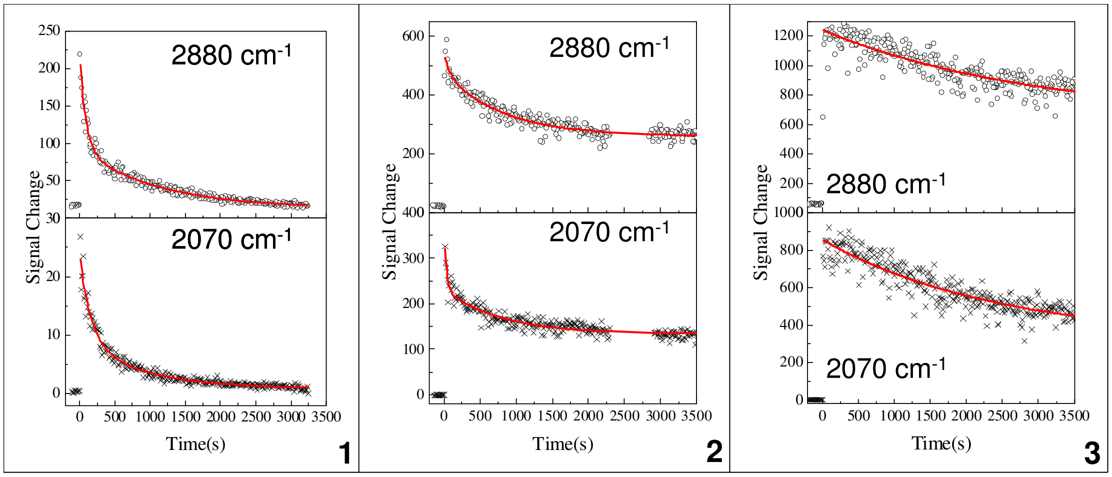

Figure 2.2. Decrease in CH_3,ss (top plots) and CD_3,ss (bottom plots) of asymmetric lipid bilayer, consisting of a dDPPG inner leaflet and a mixed 1% polymer-DPPG outer leaflet, over time. Polymer **1** is on the left, polymer **2** is in the middle, and polymer **3** on the right.

polymers **1** and **2** have a quick decrease in both signals followed by a much slower decrease, while polymer **3** only exhibits the slow decline of signal. It is believed that SFG signal decreases as a function of time because of the flip-flop of the two leaflets in the bilayer. Our control experiments show that SFG signal from a dDPPG/DPPG bilayer would not decrease for tens of hours, showing that such a bilayer is stable and no flip-flop occurs. When a small amount of the polymer is included in the outer leaflet, the lipid bilayer becomes unstable, and flip-flop occurs. It is thought that the faster the SFG signal decreases, the stronger interaction between the lipid bilayer and the polymer occurs.

Using an exponential decay the time-dependent SFG signal decrease can be fitted. Then the fitting constant which characterizes the SFG signal decay rate can be used to compare the interactions of the different polymers with the lipid bilayer. From Table 2.1 it can be seen that Polymer **1** and Polymer **2** generate similar decay rates for the slow portion, 8.9×10^{-4} and 12.3×10^{-4} s^{-1}, respectively for the SFG signal from the outer

Table 2.1. Rate constants for the time dependent change of the dDPPG/1% polymer-DPPG bilayers. Dividing into a faster process and a slow process.

Sample	$K_{fast}(10^{-4}\ s^{-1})$			$K_{slow}(10^{-4}\ s^{-1})$		
	CH	CD	Average	CH	CD	Average
dPG-PG 1% Polymer 1	112.4	64.9	88.6	8.9	11.6	10.3
dPG-PG 1% Polymer 2	128.4	297.6	213	12.3	12.7	12.5
dPG-PG 1% Polymer 3	N/A	N/A	N/A	3.4	4.1	3.7

hydrogenated layer, and 11.6 x10^{-4} and 12.7 x10^{-4} s^{-1}, respectively, for the SFG signal from the inner deuterated layer. The earlier, fast portion for polymers **1** and **2** however, exhibits differences between the inner and outer layers. For the outer layer, the rate is once again close for both polymers, 112.4 x10^{-4} s^{-1} for polymer **1** and 128.4 x10^{-4} for polymer **2**. However, the inner layer has very different behaviors: for polymer **1** the rate is almost half that of the outer layer at 64.9 x10^{-4} s^{-1}, while polymer **2** it is over twice the rate of the inner layer at 297.6 x10^{-4} s^{-1}. This would seem to indicate that polymer **2** has a much easier time interacting with the inner dueterated layer than polymer **1**. The different signal decay rates for the SFG signals from the outer and inner leaflets indicate that in addition to the flip-flop effect, polymers may disrupt the outer and inner leaflets in a different way.

In comparison, polymer **3** seems to exhibit weaker interaction with either leaflet. The lack of a fast process could be due to an absence of substantial disruption in the bilayer. Examining the slow process does not alleviate the picture at all as the smaller rates for both the inner and outer layer, 3.4 x10^{-4} and 4.1 x10^{-4} s^{-1} could also result from either behavior, but it is most likely due to flip-flop as it occurs at a similar rate.

The similarities and differences between the three polymers are not unexpected. Polymers **1** and **2** lack a fluorinated portion while polymer **3** includes a short fluorinated chain as well as having slightly more pyridinium rings. Antibacterial assays done previously with *S. aureus* show that polymer **3** exhibits a greater degree of antimicrobial behavior than polymer **1** or an analog to polymer **2**. The increased antimicrobial behavior was thought to result from the ability of the polymer to disrupt the cell membrane, causing an increase in cell death versus the other samples.[5] It appears that the anti-fouling measurements cannot be well correlated to the SFG data presented here. Clearly polymers **1** and **2** interact with model cell membranes more strongly. Perhaps cell membrane disruption is not the only reason for anti-fouling activity to occur.

2.3.2 SFG Measurements on Polymers Deposited on Fused Silica Windows

SFG spectra of surfaces of polymers **1**, **2**, and **3** deposited on fused silica windows were collected in face-down geometry (Figure 1.3A) in air (Figure 2.3) and in contact with D_2O (Figure 2.4). The ssp spectrum from polymer **1** surface in air has dominating peaks from the symmetric CH_3 stretch at ~2880 cm^{-1} and its Fermi resonance at ~2940 cm^{-1}. There is also a shoulder at ~2850 cm^{-1} attributed to the symmetric CH_2 stretch. In both ppp and sps SFG spectra, the asymmetric CH_3 stretch at ~2970 cm^{-1} can be seen with varying intensities. The SFG ssp spectrum of Polymer **2** is also dominated by the symmetric CH_3 stretch and it's Fermi resonance, as well as having the shoulder from the symmetric CH_2 stretch. However, it also has a shoulder at ~2915 cm^{-1} arising from the asymmetric CH_2 stretch along with a weak peak at ~3065 cm^{-1} arising from the ν_2 phenyl stretching mode. The ppp spectrum contains the asymmetric CH_3 stretch like polymer **1**, but also has a weak asymmetric CH_2 stretch signal. The sps spectrum contains the same stretches as the ppp spectra for polymer **2** just with weaker intensities. The SFG ssp spectrum of polymer **3** contains the same stretching modes as polymer **2** except for the ν_2

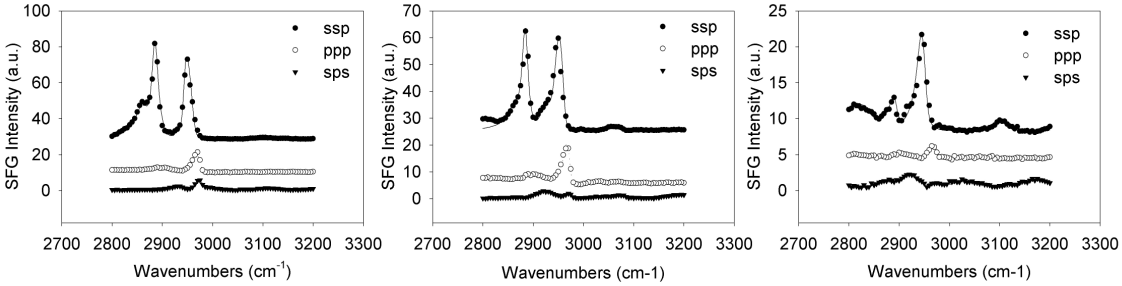

Figure 2.3. Polymer **1** (left), polymer **2** (middle), and polymer **3** (right) SFG spectra collected in ssp, ppp, and sps polarization combinations at the air interface in the face-down window geometry.

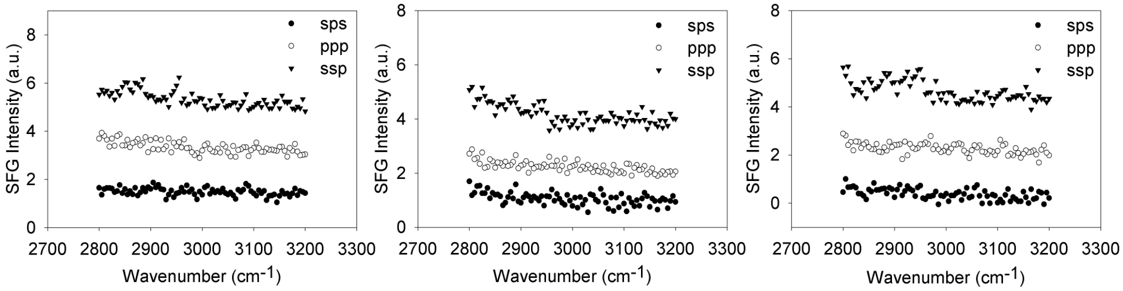

Figure 2.4. Polymer **1** (left), polymer **2** (middle), and polymer **3** (right) SFG spectra in the ssp, ppp, and sps polarizations at the D_2O interface in the face-down window geometry.

phenyl stretching mode. However, the intensity of the symmetric CH_3 stretch is much weaker than both polymers **1** and **2** and the asymmetric CH_2 stretch is much more intense. There is also a peak at 3120 cm^{-1} of curious origin. The position is too high for normal phenyl modes and remains unassigned at this point. The ppp spectrum is again dominated by the asymmetric CH_3 stretch, while the sps spectrum is dominated by the asymmetric CH_2 stretch.

SFG spectra collected in air from polymers **1** and **2** are more similar to each other compared to that from polymer **3**. The stronger asymmetric CH_2 in polymer **3** is most likely indicative of greater disruption in the alkyl side chains, possibly resulting from the desire of the more hydrophobic fluorinated portion to be at the surface. Polymers **1** and **2** are able to allow the CH_3 terminal groups to dominate the surface; resulting in the strong symmetric stretching signals in ssp. Polymer **2** has phenyl side chains, which are detected on the surface in air.

As shown in Figure 2.4, attempts to collect SFG spectra from the buried polymer/D_2O interface were unsuccessful and no discernable signal was detected. As the desired use of these polymers is ultimately for anti-fouling, learning their surface behavior in an aqueous environment is more important than understanding the static behavior in air. In order to increase the signal, a TIR prism geometry was adopted and experimental results will be discussed in greater detail in the next section.

2.3.2 SFG Measurements on Calcium Fluoride Prisms

Using the polymers spin-coated on prisms, SFG spectra of polymers **1**, **2**, and **3** were collected using a TIR prism geometry (Figure 1.3C) in both air (Figure 2.5) and D_2O (Figure 2.6). Comparison between the spectra collected in face-down window geometry and TIR prism geometry shows that there are significant differences between the two geometries, especially in the ppp spectrum.

In the case of polymer **1** additional two peaks are present in the ppp spectrum. These peaks coincide with the symmetric CH_3 stretch and it's Fermi resonance. Polymer **2** exhibits a similar trend. Also, in both cases, the peaks resulting from the CH_2 symmetric and asymmetric stretches are not present in the ssp spectra. The sps spectrum for polymer **1** only varies in the intensity of the asymmetric CH_3 stretch between the window and prism geometries. However, while polymer **2** still shows the asymmetric CH_3 stretch, the asymmetric CH_2 is absent and instead the symmetric CH_2 and symmetric CH_3 stretches are present. These results are inconsistent with typical SFG measurements

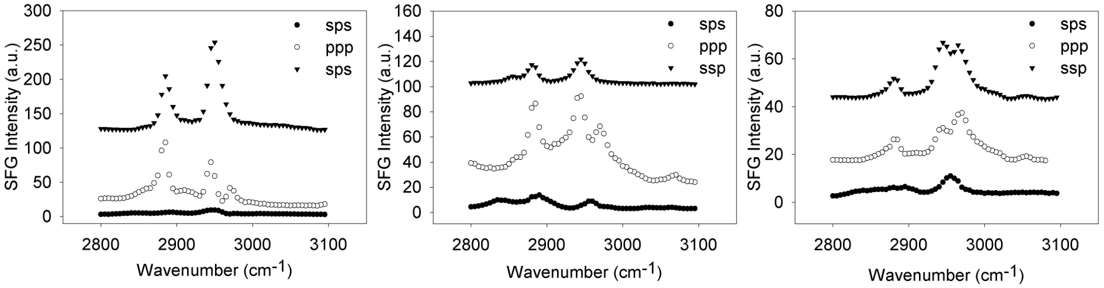

Figure 2.5. Polymer **1** (left), polymer **2** (middle), and polymer **3** (right) SFG spectra in the ssp, ppp, and sps polarizations at the air interface in the TIR prism geometry.

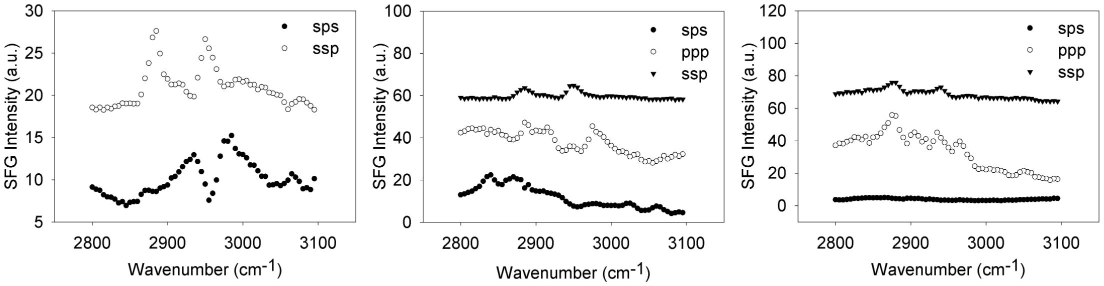

Figure 2.6. Polymer **1** (left), polymer **2** (middle), and polymer **3** (right) SFG spectra in the ssp, ppp, and sps polarizations at the D_2O interface in the TIR prism geometry.

as the ssp polarization is generally more sensitive to the symmetric stretches, due to the dipole and the IR polarization being in the same plane (and usually methyl groups like to stand up in air). Likewise, for sps spectrum the asymmetric stretching transitional dipole moments are in plane with the s-polarized IR.

For polymer **3**, the trend of seeing symmetric stretches in the ppp polarization continues. The sps spectrum, while different when compared to that from the window geometry, the primary peak is still the asymmetric CH_3 stretch in both, which is expected. However, in the ssp polarization the biggest difference is observed. There is a very strong asymmetric CH_3 stretching peak right next to a strong CH_3 Fermi resonance.

It can clearly be seen that between the window geometry and the prism geometry there is a significant change in the measured SFG signal, more than likely resultant from the change in geometry. The probable reason is due to the SFG signal that can be generated at the substrate/polymer buried interface. In face-down window geometry the strength of the SFG signal from the buried interface is very weak as most of it is transmitted through the window and not reflected so it can be neglected. In the prism geometry this buried interface may or may not contribute depending on the materials. For the case of polymers **1**, **2**, and **3** it is apparent that the buried interface does contribute significantly resulting in a much more complicated picture.

Upon contacting D_2O, the SFG signal strength becomes much weaker, but it is still measurable. For polymer **1**, the symmetric CH_3 stretch with it's Fermi resonance are still present in the ssp polarization, while the asymmetric CH_2 and asymmetric CH_3 stretches are present in sps. There is also some weak CH_3 symmetric stretching signal and ν_2 phenyl signal in the sps spectrum. Polymer **2** has a very similar spectrum to polymer **1** in ssp when contacted D_2O. However, the sps spectrum contains primary contributions from the CH_3 and CH_2 symmetric stretches. There may be further contributing signals but a strong O-D stretch results in a background that makes it hard to say with certainty what they are. Again, polymer **3** exhibits weak symmetric CH_3 and Fermi resonance in the ssp polarization. For sps there is no detectable signal. Due to the aforementioned contribution from the buried interface, it is difficult to conclude that the signals generated while the polymer surface was contacted D_2O arise solely from that interface or if some of the signals are from the buried polymer/prism interface.

2.3.4 Polymer 3 on prism in the C-F Stretching Region

As polymer **3** has a partially fluorinated side chain, an attempt to gather spectra from the C-F stretching region was made in order to better elucidate what was occurring between the alkyl and fluorinated side chains. As can be seen in Figure 2.7, there is a strong peak at ~1440 cm^{-1} and a much weaker peak at ~1180 cm^{-1}. The peak at ~1180 cm^{-1} is tentatively assigned to one of the CF_2 asymmetric stretching modes. The ~1440 cm^{-1} peak, however, has no assignment that is consistent with C-F stretching literature. Upon examination of a cleaned CaF_2 prism this peak is still observed, therefore it is contributed by the CaF_2. This peak does cause some problems as there is a C-F stretching mode present at 1370 cm^{-1} that can be partially or completely obscured by the presence of the CaF_2 substrate peak at ~1440 cm^{-1}.

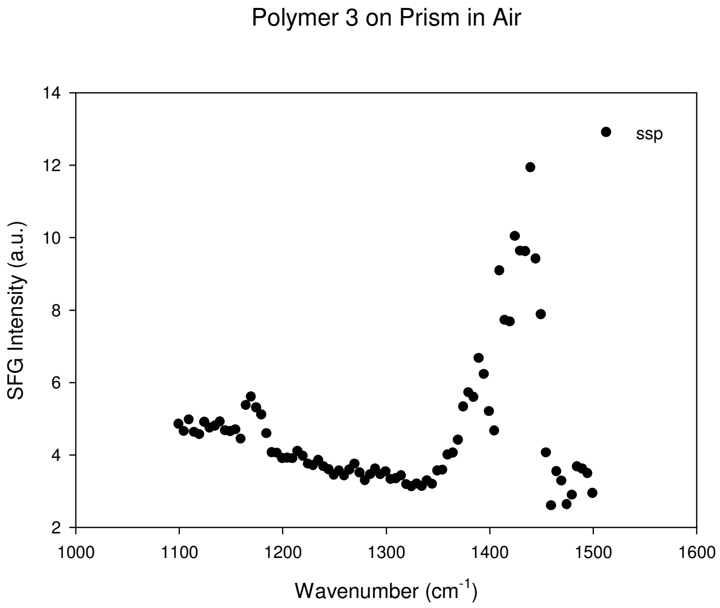

Figure 2.7. SFG spectrum of Polymer **3** in ssp polarization in the TIR prism geometry in C-F stretching region

2.4 CONCLUSIONS

From the lipid bilayer studies, as well as the spectra of the polymers in air on windows, it can be seen that polymers **1** and **2** behave in a similar fashion. The presence of the fluorinated groups on polymer **3** results in significantly different behavior. The fluorinated group gives polymer **3** a different surface structure that results in a different

SFG spectrum in air as well as a lack of a fast SFG signal decay step while interacting with a lipid bilayer.

It is difficult to observe any SFG signal from the polymer surfaces in water using polymer films deposited on fused silica windows. Using polymers on prisms with the TIR experimental geometry, SFG signals can be detected from polymer surfaces in water. However, it seems that such signals are contributed by polymer surfaces in water and buried polymer/substrate interfaces. It is apparent that in order to better understand the behavior of these polymer surfaces in water, finding a way to separate the SFG signal contributed by the buried interface from the exposed surface is necessary. Before attempts could be made with this set of polymers, the Ober group had developed a new set of material with improved anti-biofouling activity. Taking what was learned using polymers **1**, **2**, and **3,** it was then decided to study the new polymer to separate signals from the polymer surface in air or water from those from the polymer/substrate interface, which will be discussed in the following chapter.

2.5 REFERENCES

(1) Waschiniskia, C. J.; Tiller, J. C. *Biomacromolecules* **2005**, *6*, 235-243.

(2) Ivanov, I.; Vemparala, S.; Pophristic, V.; Kuroda, K.; DeGrado, W. F.; McCammon, J. A.; Klein, M. L. *J. Am. Chem. Soc.* **2006**, *128*, 1778-1779.

(3) Kügler, R.; Bouloussa, O.; Rondelez, F. *Microbiology* **2005**, *151*, 1341-1348.

(4) Tiller, J. C.; Liao, C.-J.; Lewis, K.; Klibanov, A. M. *Proc. Natl. Acad. Sci U.S.A.* **2001**, *98*, 5981-5985.

(5) Krishnan, S.; War, R. J.; Hexemer, A.; Sohn, K. E.; Lee, K. K.; Angert, E. R.; Fischer, D. A.; Kramer, E. J.; Ober, C. K. *Langmuir* **2006**, *22*, 11255-11266.

(6) Chen, X.; Tang, H.; Even, M. A.; Wang, J.; Tew, G. N.; Chen, Z. *J. Am. Chem. Soc.* **2006**, *128*, 2711-2714.

(7) Chen, X.; Wang, J.; Boughton, A. P.; Kristalyn, C. B.; Chen, Z. *J. Am. Chem. Soc.* **2006**, *129*, 1420-1427.

CHAPTER 3: SURFACE STRUCTURES OF AN AMPHIPHILIC TRI-BLOCK COPOLYMER IN AIR AND IN WATER PROBED USING SUM FREQUENCY GENERATION VIBRATIONAL SPECTROSCOPY

3.1 INTRODUCTION

The new coating examined in this chapter is based on an amphiphilic block copolymer system developed by Ober and coworkers.[1,2] Ober *et al.* were able to create a polymer with antifouling and fouling release properties by combining both grafted hydrophobic fluoroalkyl and grafted hydrophilic ethylene glycol groups. This approach produced a polymer with a dynamic, responsive surface, capable of both resisting and easily releasing fouling organisms.[2,3] Another important feature enabling anti-fouling/fouling release is a low Young's modulus.[4] In order to control the modulus of the surface coating, a thick layer of polystyrene-*block*-poly(ethylene-*ran*-butylene)-*block*-polystyrene (SEBS) was used as an anchoring layer for a amphiphilic surface active triblock copolymer (SABC) containing a polystyrene-b-poly(ethylene-*ran*-butylene) sequence matched to the SEBS. This enables the fluorinated and PEGylated surface active groups of the SABC to be present at the surface while maintaining a low Young's modulus.

Here, the surface structures of the SABC developed by the Ober group derived from polystyrene$_{8K}$-*block*-poly(ethylene-*ran*-butylene)$_{25K}$-*block*-polyisoprene$_{10K}$ (PS$_{8K}$-*b*-P(E/B)$_{25K}$-*b*-PI$_{10K}$) tri-block copolymer precursor functionalized with ethoxylated fluoroalkyl groups on the polyisoprene block (Figure 3.1) will be discussed.[2] The surface

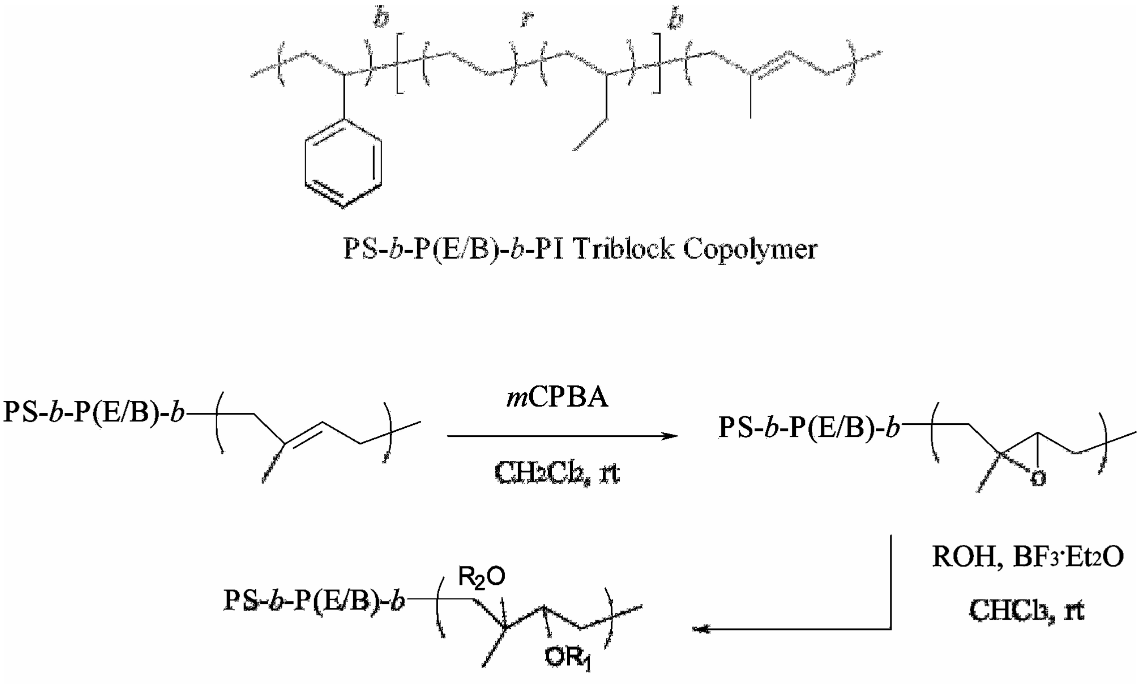

R_1, R_2 = H or R, where R = $-CH_2CH_2(OCH_2CH_2)_x(CF_2CF_2)_yF$

Figure 3.1. Molecular formula for SABC (Reproduced with permission from *Langmuir* **2009**, *25* 12266-12274. Copyright 2009 Am. Chem. Soc.). The polystyrene block has a molecular weight of ~8 kilodaltons. The random ethylene-butylene block has a molecular weight of ~25 kilodaltons. The isoprene block has a molecular weight of ~10 kilodaltons with an R group with x=3.5 and y=5.

structures of the SABC in air and water were examined by SFG through the use of films with varying thicknesses, as was done in previous studies involving buried polymer/metal interfaces.[5,6] It was found that the SFG spectra generated in the alkyl C-H stretching frequency region are a combination of both the buried substrate/SABC interface as well as the SABC at the air or aqueous interface. The presence of fluorinated groups in air as well as in D_2O was detected and this is the first case of fluorinated signal observation by SFG of a polymer material in contact with an aqueous environment. As fluorinated materials are of increasing interest to the polymer community, it is important to be able to observe their behavior at a water interface.

3.2 EXPERIMENTAL

3.2.1 Sample Preparation

The synthesis of the SABC has been given in detail previously.[2] The SABC triblock copolymer was dissolved in chloroform (Sigma) in a 1% wt/wt solution. The samples were then prepared by spin coating (Specialty Coatings Systems) at 500 rpm intervals from 500-3000 rpm onto one leg of a CaF_2 right angle prism (Altos) to create a series of polymer films with different thicknesses. Deuterated water (D_2O) was obtained from Sigma Aldrich and used to avoid water bands overlapping the primary C-H stretching signals. The film thicknesses were measured with a Dektek 3 profilometer from Veeco. For each sample, 3-4 measurements were made and then averaged.

3.2.2 SFG

SFG is a second order nonlinear spectroscopy technique that has proven powerful in probing surfaces and interfaces. The full theory of this method has been discussed Chapter 1. For the SFG experiments in this chapter, the SABC coated CaF_2 prisms were mounted as shown in Figure 1.3C. The polarization combination used was ssp. For the spectrum collected with the SABC in contact with D_2O the time of contact was approximately 30 minutes. No changes in the spectrum as a function of time in contact with D_2O were observed.

3.3 RESULTS AND DISCUSSION

3.3.1 SFG Measurements of SABC in Air in C-H Stretching Region

SFG ssp spectra of a series of SABC samples with different film thicknesses were collected in air and are displayed in Figure 3.2. The peak assignments of C-H stretching modes have been extensively studied.[11,12] Two dominant peaks, each with a shoulder, and one weaker peak can be observed in the spectra. The peak at ~2880 cm^{-1} is attributed to the symmetric stretch of the CH_3 group in the amphiphilic polyisoprene block. The polymer chain end methyl groups have a much lower overall concentration; therefore they are not likely to be the dominant groups to contribute this signal. The other dominant peak at ~2950 cm^{-1} is attributed to the CH_3 Fermi resonance. The shoulder found between these two peaks is a result of the asymmetric CH_2 stretch centered at ~2910 cm^{-1}. The CH_3 asymmetric stretching signal centered at ~2960 cm^{-1} appears as a shoulder or as a tail of the Fermi resonance. Lastly, there is a weak peak found at ~2840 cm^{-1} that arises from the symmetric stretch of the CH_2 group. Both methylene signals can be contributed from all the methylene groups in the molecule. As the thickness of the thin film increases, the intensity of the SFG signal decreases. If the polymer/air interface dominates, then there should be no SFG signal dependence on thickness. Thus, there exists a second

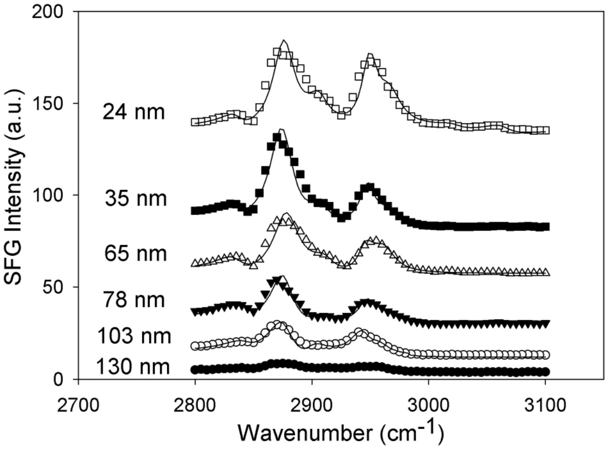

Figure 3.2. SFG spectra of SABC films with varying thicknesses in the ssp polarization in contact with air. Spectra are offset for clarity.

interface where the inversion symmetry can be broken, the CaF_2/polymer buried interface. For many polymers, SFG signals generated from this interface are negligible,[7] but in this system, the additional interface generates some SFG signals which cannot be ignored. The SFG signals detected in Figure 3.2 might be from a contribution from two interfaces (the polymer/air and the CaF_2/polymer interfaces), or even solely by the CaF_2/polymer interface.

In order to determine where the SFG signal is coming from, the Fresnel coefficients of both interfaces were compared. As stated before, the SFG signal is related to $\chi_{eff}^{(2)}$ and, therefore, to the Fresnel coefficients. The Fresnel coefficients may vary for the two interfaces when the sample thickness changes. By examining the Fresnel coefficients of both interfaces the source(s) of the SFG signal could be determined. Using the detailed analysis presented next, thickness dependent curves of the Fresnel coefficients of the two interfaces were generated.

The prism geometry for the SFG experiment with pertinent angles labeled is shown in Figure 3.3. Media 0, 1, and 2 represent the air, CaF_2 prism, and SABC, respectively. Medium 3 represents the medium contacting with the K3A-SU7 surface. In this research, air and water are used as medium 3. The indices of refractions used for the following calculations are shown in Table 3.1.

The input beams go through the first 0-1 interface, propagate inside the prism, and then propagate to the 1-2 interface. Here, for simplicity the visible and infrared beams are treated as having the same input angle. The SABC thin film (medium 2) between the CaF_2 and medium 3 can be taken as a nonlinear polarization sheet and thus the SFG signal can be generated. The generated sum frequency beam propagates inside the CaF_2

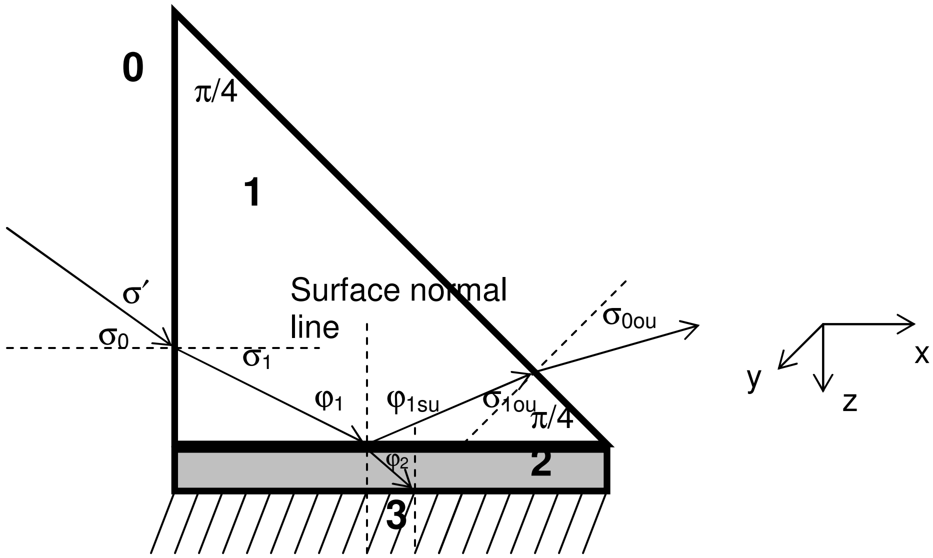

Figure 3.3. Diagram of angles used in calculation for the determination of the Fresnel coefficient thickness dependence curves.

Table 3.1. Indices of refraction used in calculations of thickness dependent Fresnel coefficients.

	461 nm	496 nm	532 nm	3472 nm, (2880 cm^{-1})	7299 nm, (1370 cm^{-1})
CaF_2 Prism	1.44	1.44	1.44	1.42	1.35
Polymer	1.47	1.47	1.47	1.47	1.47
Air	1	1	1	1	1
H2O	1.33	1.33	1.33	1.32	1.31
Prism/Polymer	1.46	1.46	1.46	1.45	1.41
Polymer/Air	1.18	1.18	1.18	1.18	1.18
Polymer/Water	1.40	1.40	1.40	1.40	1.39

prism and then goes through the 1-0 interface to reach the detector.

As a starting point the input beams transmitting the 0-1 interface are considered. σ'_0 is already known (π/3 for visible beam and 3π/10 for infrared beam in radians). The σ_0 taken can be determined from $\sigma_0=\pi/2-\sigma'_0$. Then the refraction angle, σ_1, can be obtained from the Snell's equation at the 0-1 interface.

$$\sigma_1 = \arcsin\left(\frac{n_0}{n_1}\sin\sigma_0\right) \tag{3.1}$$

The incidence angle at the 1-2 interface φ_1 can thus be obtained from $\varphi_1=\pi/2-\sigma_1$. The SFG signal is generated from the polymer thin film. Here, two interfaces, the CaF$_2$/polymer and polymer/medium 3 interfaces exist. A thin-film model was used to calculate the Fresnel coefficients of the two interfaces.[5,8-10]

For the CaF$_2$/polymer interface

$$L_{xx}^{\mathrm{Pr}ism/Polymer}(\omega_i)=t^p\left(1-r_{23}^p e^{2i\beta}\right)\frac{\cos(\varphi_2)}{\cos(\varphi_1)} \tag{3.2}$$

$$L_{yy}^{\mathrm{Pr}ism/Polymer}(\omega_i)=t^s\left(1+r_{23}^s e^{2i\beta}\right) \tag{3.3}$$

$$L_{zz}^{\mathrm{Pr}ism/Polymer}(\omega_i)=t^p\left(1+r_{23}^p e^{2i\beta}\right)\frac{n_1 n_2}{n_{\mathrm{Pr}ism/Polymer}^2} \tag{3.4}$$

ω_i is the input beam frequency; t_p and t_s are the overall transmission coefficients at the prism/polymer interface for the p- and s- polarized lights, respectively; r_{23} is the linear reflection coefficient at the polymer/medium 3 interface; β is the phase difference when the input beam propagates across the polymer thin film. φ_1 and φ_2 are the beam incidence angles in the prism and polymer, respectively. n_1 and n_2 are refractive indices of the prism and polymer, respectively. $n_{Prism/Polymer}$ is the refractive index of the polymer interfacial layer at the prism/polymer interface.[5]

$$t^p=\frac{t_{12}^p}{1+r_{12}^p r_{23}^p e^{2i\beta}} \tag{3.5}$$

$$t^s=\frac{t_{12}^s}{1+r_{12}^s r_{23}^s e^{2i\beta}} \tag{3.6}$$

$$\beta=\frac{2\pi}{\lambda_0}n_2 d\cos\varphi_2 \tag{3.7}$$

t_{12}, r_{12}, and r_{23} are the linear transmission and reflection coefficients.

For the polymer/medium 3 interface[5]

$$L_{xx}^{Polymer/Medium3}(\omega_i) = t^p e^{i\beta}\left(1 - r_{23}^p\right)\frac{\cos(\varphi_2)}{\cos(\varphi_1)} \tag{3.8}$$

$$L_{yy}^{Polymer/Medium3}(\omega_i) = t^s e^{i\beta}\left(1 + r_{23}^s\right) \tag{3.9}$$

$$L_{zz}^{Polymer/Medium3}(\omega_i) = t^p e^{i\beta}\left(1 + r_{23}^p\right)\frac{n_1 n_2}{n_{Polymer/Medium3}^2} \tag{3.10}$$

where $n_{Polymer/Medium3}$ is the refractive index of the polymer interfacial layer at the polymer/medium 3 interface. The equations for the output sum frequency beam in the reflection geometry for both the prism/polymer and polymer/medium 3 interfaces can also be obtained for the experimental geometry employed, which have the same form as those for the input beams.[9]

The output sum frequency beam propagates in the prism and then goes through the 1-0 interface. Supposing the output sum beam angle at the 1-2 interface is φ_{1su}, the output angle at the 1-0 interface before the sum frequency beam transmits this interface is $\sigma_{1out}=\varphi_{1su} - \pi/4$. So the output angle after the sum frequency beam transmits this interface is

$$\sigma_{0out} = \arcsin\left(\frac{n_1}{n_0}\sin\sigma_{1out}\right) \tag{3.11}$$

For the ssp polarization combination, since the angle relationship at the input 0-1 and output 1-0 interfaces are known, respectively, the linear Fresnel coefficients for the two input beams at the 0-1 interface (air/CaF_2) and one output beam at the 1-0 interface (CaF_2/air) can be taken into account. Finally, the overall Fresnel coefficients before the second-order nonlinear susceptibility tensor components for ssp polarization combination can be deduced, resulting in[5]

$$F_{yyz}^{Prism/Polymer} = L_{yy}^{Prism/Polymer}(\omega)\cdot t_s^{10}(\omega)\cdot L_{yy}^{Prism/Polymer}(\omega_1)\cdot t_s^{01}(\omega_1) \\ \cdot L_{zz}^{Prism/Polymer}(\omega_2)\cdot t_p^{01}(\omega_2)\cdot \sin\varphi_1^{infrared} \tag{3.12}$$

$$F_{yyz}^{Polymer/Medium3} = L_{yy}^{Polymer/Medium3}(\omega)\cdot t_s^{10}(\omega)\cdot L_{yy}^{Polymer/Medium3}(\omega_1)\cdot t_s^{01}(\omega_1) \\ \cdot L_{zz}^{Polymer/Medium3}(\omega_2)\cdot t_p^{01}(\omega_2)\cdot \sin\varphi_1^{infrared} \tag{3.13}$$

From these equations plots can be generated for the thickness effect on the Fresnel coefficients at both the CaF_2/polymer and polymer/air (D_2O) interfaces, which are used throughout this chapter.

For the polymer/air interface, it can be seen that there is little change in the value of the Fresnel coefficients in the thickness range under study (Figure 3.4). The Fresnel coefficients grow from 0.683 at 24 nm to 0.811 at 130 nm, an increase of ~18%. This means as the thickness of the film increases, the Fresnel coefficients increase. This should lead to an increase in SFG signal, which is not what was observed. Taking the strength over the width of the symmetric stretching peak from the fit parameters (Table 3.2) an indication of the relative value of the symmetric stretch for each thickness is generated. As the thickness increases, the value goes from 7.73 at 24 nm to 2.31 for 130 nm, a drop of ~77% percent. So not only is the change in Fresnel coefficients trending in the opposite way, but the magnitude of the calculated trend (18% change) is almost four times less than the experimentally observed results (77% change).

As the thickness dependent SFG signal strength from the polymer/air interface does not adequately explain the results, the Fresnel coefficients of the CaF_2/polymer interface were calculated. For the CaF_2/polymer interface, the Fresnel coefficients are

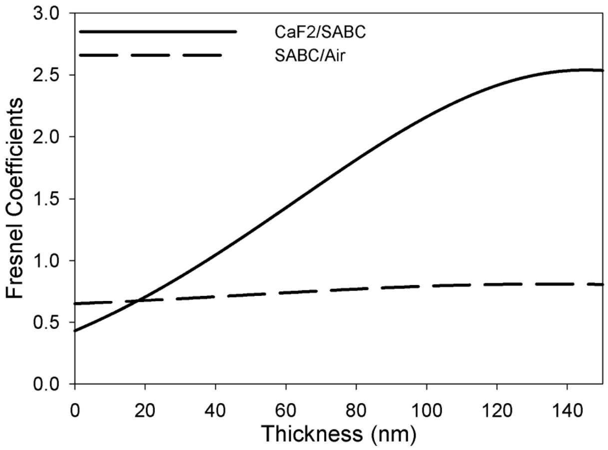

Figure 3.4 Fresnel coefficients as a function of thickness for the CaF_2/SABC interface and the SABC/Air interface at 2880 cm^{-1}.

Table 3.2. Fit parameters for SABC in Air in the C-H stretching frequency region. A, x, and w are signal strength, peak center, and peak width respectively.

Thickness(nm)	24	35	65	78	103	130
NR	-1.4	-2	-1.3	-1.9	-1.9	-0.5
A1	12	18	20	20	11	11
x01	2836	2834	2835	2840	2843	2843
w1	10	13	13	13	13	13
A2	85	95	80	68	64	30
x02	2876	2875	2878	2876	2876	2875
w2	11	12	13	12	13	13
A3	-63	-53	-46	-41	-42	-26
x03	2906	2906	2912	2905	2900	2915
w3	11	10	11	11	10	13
A4	69	60	48	55	65	35
x04	2949	2948	2945	2948	2944	2952
w4	8	8	8	8	10	12
A5	-76	-65	-60	-58	-59	-26
x05	2967	2962	2962	2958	2955	2965
w5	12	12	12	10	10	12
A6	8	0	0	0	0	0
x06	3025	3020	3020	3020	3025	3025
w6	12	12	12	12	12	12
A7	16	0	0	0	0	0
x07	3065	3050	3050	3050	3055	3050
w7	12	12	12	12	12	12

seen to change to a much greater degree than the polymer/air interface (Figure 3.4). At 24 nm the CaF_2/polymer Fresnel coefficient is 0.755, which increases to 2.50 at 130 nm.

This is an increase of >300%, which would indicate for a film of 130 nm in thickness, the buried interface signal strength should be over 3 times stronger (intensity will be 9 times stronger) than that found for a film of 24 nm. This value is much closer to the magnitude of change seen in the collected spectra, but once again the trend is in the opposite direction. According to the Fresnel coefficients for both interfaces, the signal should increase from both interfaces as the thickness increases.

The SFG data follows neither trend when considering only one interface at a time, thus it may be possible that SFG signals are generated from both interfaces and they are somehow interfering with each other. For the case of interference between the two interfaces, the SFG intensity can be related as follows[5-7]

$$I_{SFG} \propto |a\times F_{Polymer/Air} + b\times F_{CaF2/Polymer}|^2 \qquad (3.14)$$

This means that some values of "a" and "b" may fit the trend of the signal strength dependence on film thickness of the experimental data. It is clear that "a" and "b" can be considered as "$\chi_{Polymer/Air}$" and "$\chi_{CaF2/Polymer}$", respectively. Apparently, "$\chi_{Polymer/Air}$" or "a" and "$\chi_{CaF2/Polymer}$" or "b" would not change as a function of sample thickness, but "$F_{Polymer/Air}$" and "$F_{CaF2/Polymer}$" are different when the sample thicknesses are varied, as shown in Figure 3.4. Here, the SFG spectra for samples with different thicknesses are fitted. From the fitting, it is possible to detect values of $a\times F_{Polymer/Air} + b\times F_{CaF2/Polymer}$ at different sample thicknesses, which are plotted as dots in Figure 3.5. The values of $a\times F_{Polymer/Air} + b\times F_{CaF2/Polymer}$ were calculated using known "$F_{Polymer/Air}$" and "$F_{CaF2/Polymer}$" values (plotted in Figure 3.4) of samples with different thicknesses and different trial values of "a" and "b". A plot of curves using various "a" and "b" values and the experimental data generated from the fit parameters can be seen in Figure 3.5. When a =

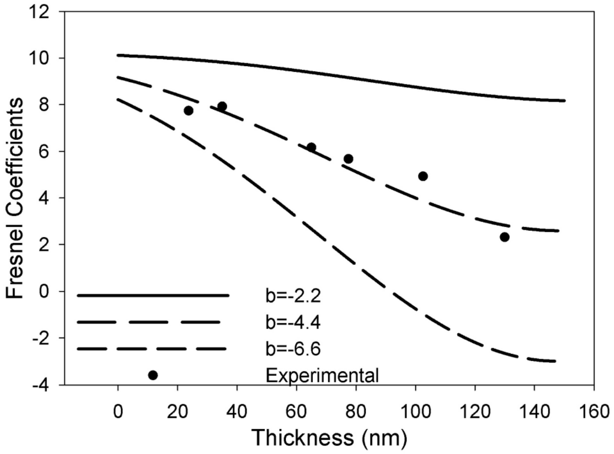

Figure 3.5. Lines: Plot of the signal strength for the symmetric stretch of CH_3 functional group of SABC films as a function of thickness using known Fresnel coefficients of the SABC/Air interface and the CaF_2/SABC interface, and trial values of "a" and "b". Dots: experimental data. When "a" is set at 17, and "b" is varied, experimental values for $\chi_{eff}^{(2)}{}_{ssp}$ fit best when b = -4.4.

17 and b = -4.4, the thickness dependent relationship between the Fresnel coefficients for both interfaces approaches the experimental data, the different signs (positive and negative) of "a" and "b" indicate a difference in the absolute orientation of the methyl groups at the two interfaces. For the polymer/air interface, it is believed that the methyl groups adopt an orientation pointing away from the surface towards the air, similar to those on other polymer (e.g., PBMA) surfaces in air, because both methyl groups and air are hydrophobic. At the CaF_2/polymer buried interface, the methyl groups point away from the bulk of the film toward the substrate. This results in methyl groups pointing in opposite directions and their SFG signals destructively interfering with each other. The difference in magnitude of the two constants is an indication of the different amplitudes of the second order nonlinear optical susceptibility components ("$\chi_{Polymer/Air}$" vs. "$\chi_{CaF2/Polymer}$"). The polymer/air interface is almost four times stronger than the buried CaF_2/polymer interface, indicating that the amplitude of the second order nonlinear

optical susceptibility component at the polymer/air interface is larger. This observation could be due to an increase in the surface coverage of the methyl groups, greater ordering (a narrower orientation distribution) of the methyl groups, or the polymer/air methyl groups having a smaller angle to the surface normal (stand up). As the sample thickness increases, the buried interface signal strength begins to increase due to the increase of the Fresnel coefficient (Figure 3.4), which results in the decrease in the observed SFG signals due to the destructive interference between signals from the two interfaces.

3.3.2 SFG Measurements of SABC in D_2O in C-H Stretching Region

Upon contacting the SABC films with D_2O, a conformational change can be observed. As seen in Figure 3.6, the symmetric CH_3 stretching and Fermi resonance signals are no longer the dominant peaks. The asymmetric CH_2 (~2930 cm^{-1}) signal is the strongest peak, which is an indication of gauche defects developing in the polymer chains at the surface or more ethylene glycol groups migrating to the surface because they are more hydrophilic. The second peak (centered at ~2955 cm^{-1}) that overlaps with the asymmetric CH_2 stretching peak is from the asymmetric CH_3 stretch. The symmetric

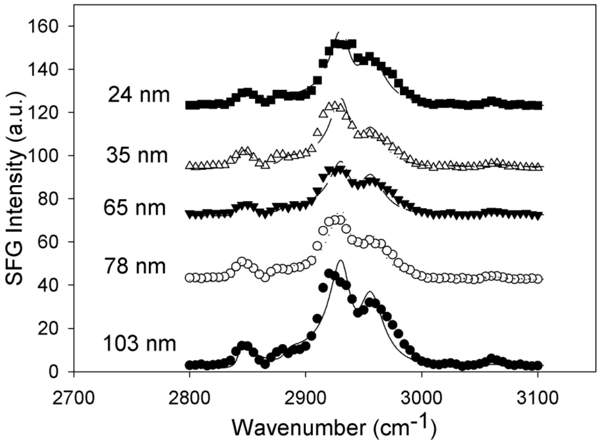

Figure 3.6. SFG spectra of SABC films of varying thickness contacted to D_2O in the ssp polarization. Spectra are offset for clarity.

CH_2 stretching signal (~2845 cm^{-1}) is still present, as is the CH_3 symmetric stretching signal (~2880 cm^{-1}), as a shoulder to the asymmetric CH_2. The change in signal intensities of the different methyl stretches is most likely a result of the methyl groups adopting a large angle to the surface normal to minimize interactions with the hydrophilic D_2O, this is confirmed by the data analysis below. It is also apparent that there is a much smaller variation of the signal intensity between the different thickness samples.

For the Fresnel coefficients of the polymer/D_2O interface, there is very little variation in the values for films with different thicknesses. At 24 nm the Fresnel coefficient is 3.27, which decreases by ~5% to 3.12 at 103 nm (Figure 3.7). Fitting the spectra, the signal strength and width of each component stretch can be found, and those parameters are listed in Table 3.3. Using the ratio of strength over width of both the symmetric and asymmetric CH_3 stretches a gauge of how the SFG intensity changes with thickness is found. For the symmetric CH_3, stretch there is a ~123% change between 24 nm and 103 nm. For the asymmetric CH_3, the difference is less pronounced with a ~20% difference. Therefore, the experimentally observed thickness dependent signal strength does not match the calculated one when only signals from the polymer/D_2O interface are considered. Furthermore, the trends of the thickness dependent signal observed and the Fresnel coefficients are opposite. The observed signals are strongest for the thickest and thinnest samples and drop in intensity for intermediate values of film thickness. The Fresnel coefficients indicate that the opposite should be true with the film with intermediate values of thickness exhibiting the strongest signal.

Applying the same approach as discussed previously to study polymer surface in air, the Fresnel coefficients for the polymer/D_2O and buried CaF_2/polymer interface

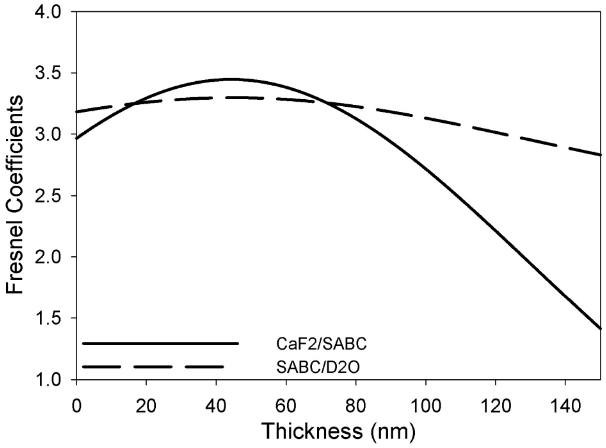

Figure 3.7. Fresnel coefficients as a function of thickness for the CaF_2/SABC interface and the SABC/D_2O interface at 2880 cm^{-1}.

Table 3.3. Fit parameters for SABC contacted to D_2O in the C-H stretching frequency region. A, x, and w are signal strength, peak center, and peak width respectively.

Thickness(nm)	24	35	65	78	103
NR	-0.1	-0.1	0	0	-0.25
A1	16	17	13	18	20
x01	2845	2845	2845	2845	2845
w1	6	6	6	6	6
A2	5	4	6	6	10
x02	2880	2879	2879	2879	2873
w2	8	8	8	8	7
A3	-51	-50	-41	-49	-60
x03	2932	2932	2932	2932	2929
w3	11	11	11	11	11
A4	-51	-42	-46	-47	-61
x04	2955	2955	2955	2955	2957
w4	13	13	13	13	13
A5	-7	-7	-6	-6	-9
x05	3025	3025	3025	3025	3025
w5	15	15	15	15	15
A6	-9	-9	-9	-8	-14
x06	3055	3055	3055	3055	3055
w6	12	12	12	12	12

(Figure 3.7) when the polymer surface is contacted D_2O are calculated. This time there is not a drastic difference between the two interfaces as was seen before. Both the buried CaF_2/polymer and polymer/D_2O interfaces exhibit the same trends with the highest values being located in the middle of the tested thicknesses. The difference is once again larger for the buried interface, but to a much lesser degree in comparison to the air case. The difference between 24 nm (3.33) and 103 nm (2.67) is ~20%. While this difference is very close to the difference for the asymmetric stretch, as stated previously, the trends do not match up.

The differences in the thickness dependent trends of the Fresnel coefficients and the observed SFG results again lead to interpreting the signals as the interference of the two interfaces as will be shown. Using Equation (3.14) a relationship that approximated our observed SFG signals for both the symmetric CH_3 and the asymmetric CH_3 stretches can be derived. In this case a = 2.6 and b = -2.4 for symmetric stretch and a = 3.3 and b = -2.1 for asymmetric stretch (Figures 3.8 and 3.9). As the signs of the two constants are again opposite, it is likely the groups have opposite absolute orientations. The buried interface should not be seeing any environment changes in comparison to that probed when the polymer is in contact with air. So the methyl groups at the polymer/CaF_2 interface will still point away from the bulk towards the polymer/CaF_2 substrate. The methyl groups at the polymer/D_2O interface are then still pointing away from the bulk into the D_2O. At this point, it is likely that the methyl groups at the polymer/water interface tilt more towards the surface, which contributes to why the constants (susceptibility components) for symmetric methyl stretch are much closer between the polymer/substrate and the polymer/water interface than those between the polymer/substrate and the polymer/air interface.

3.3.3 SFG Measurements of SABC in C-F Stretching Region

As the SABC has a short fluorinated portion on the side chain, the SFG signals generated in the C-F stretching frequency region were also examined (Figure 3.10). A

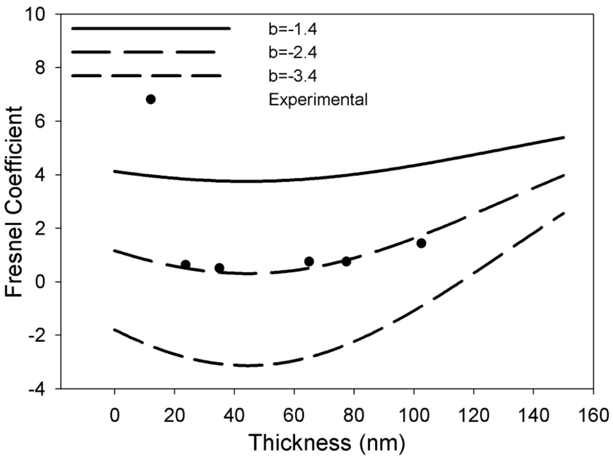

Figure 3.8. Lines: Plot of the signal strength for the symmetric stretch of CH_3 functional group of SABC films as a function of thickness using known Fresnel coefficients of the SABC/D_2O interface and the CaF_2/SABC interface , and trial values of "a" and "b". Dots: experimental data. When "a" is set at 2.6, and "b" is varied, experimental values for $\chi_{eff}^{(2)}{}_{ssp}$ fit best when b = -2.4.

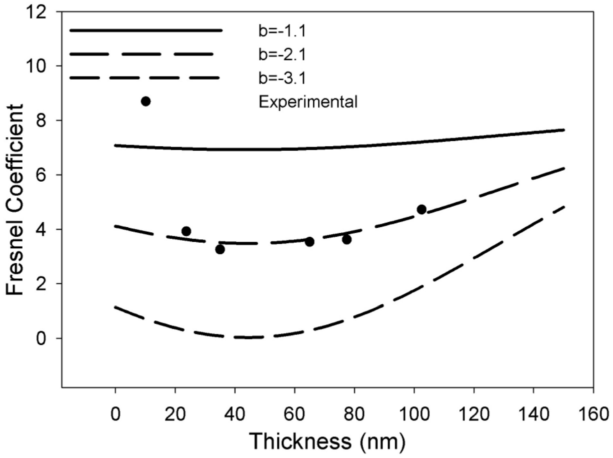

Figure 3.9. Lines: Plot of the signal strength for the asymmetric stretch of CH_3 functional group of SABC films as a function of thickness using known Fresnel coefficients of the SABC/D_2O interface and the CaF_2/SABC interface, and trial values of "a" and "b". Dots: experimental data. When "a" is set at 3.3, and "b" is varied, experimental values for $\chi_{eff}^{(2)}{}_{ssp}$ fit best when b = -2.1.

dominant peak appears at 1440 cm^{-1} which is attributed to the CaF_2 substrates. The origin of this signal is unknown, but it can be observed from the CaF_2 substrate without the polymer. There is also a shoulder that appears centered at 1380 cm^{-1}, assigned to the CF_3 asymmetric[13] or CF_2 asymmetric[14] mode. Upon first examination of the collected

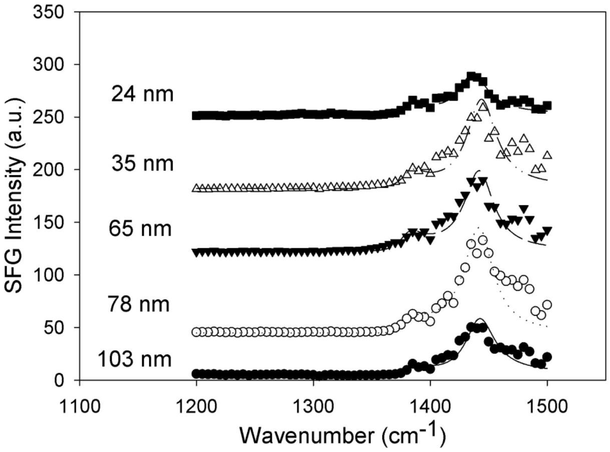

Figure 3.10. SFG spectra of SABC films of varying thickness in Air in the ssp polarization in the C-F spectral region. Spectra are offset for clarity.

SFG spectra it becomes readily apparent that there is not a large change in the signals as the polymer film thickness changes. This is different from what was seen in the C-H stretching frequency region and more in line with what is generally seen with SFG where polymer film thickness does not affect the spectra. Upon fitting the spectra (Table 3.4), it was found from the ratio of the strength to width that the largest variation was about ~25% and the decrease from 24 nm (4.3) to 103 nm (3.6) was ~16% (Table 3.5).

Table 3.4. Fit parameters for SABC in Air in the C-F region. A, x, and w are signal strength, peak center, and peak width respectively.

Thickness(nm)	24	35	65	78	103
NR	1.09	0.98	0.70	0.30	1.09
A1	-51	-54	-54	-40	-43
x01	1385	1382	1380	1380	1385
w1	12	12	12	12	12
A2	98	141	134	152	112
x02	1436	1443	1442	1442	1442
w2	15	15	15	15	15

Looking at the calculated Fresnel coefficients for polymer/air and CaF_2/polymer (Figure 3.11) interfaces, it is possible to determine if there was any interference between

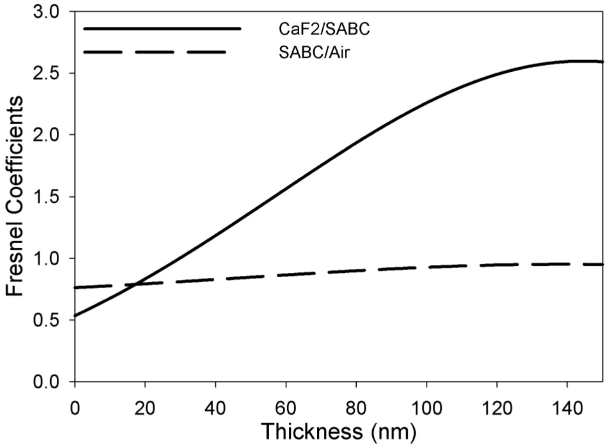

Figure 3.11. Fresnel coefficients as a function of thickness for the CaF_2/SABC interface and the SABC/Air interface at 1370 cm^{-1}.

the signals from the two interfaces. For the polymer/air case, an increase of ~16% occurs from 24 nm to 103 nm, while the CaF_2/polymer increases by >250% from 24 nm to 103 nm. As these numbers are similar to the C-H region Fresnel coefficients, it would be expected that if there were a significant interference between the two interfaces it should result in a major change in the intensity of the C-F signal. As the change in both the Fresnel coefficients for the polymer/air interface and measured results are similar, it was concluded that the buried interface contributes very little to the observed SFG signal, and the signal mainly comes from the polymer surface in air. This shows that fluorinated segments are present on the tri-block copolymer surface in air, as shown by XPS previously (in vacuum).[2]

The C-F region was also observed from polymer films in D_2O (Figure 3.12). Due to the change from air to water the 1440 cm^{-1} peak from the substrates has decreased allowing the C-F signal (1375 cm^{-1}) to be resolved cleanly. As is the case in air, in the C-F and C-H region in D_2O there is little variation with change in thickness. Examination

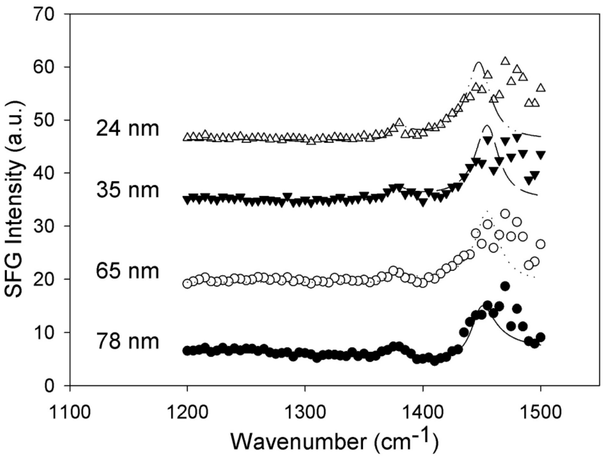

Figure 3.12. SFG spectra of SABC films of varying thickness in contact to D_2O in the ssp polarization in the C-F spectral region. Spectra are offset for clarity.

of the fit parameters (Table 3.5) for 23 nm (1.50) and 80 nm (1.25) (Table 3.6) shows a decrease in the signal of ~17% as the thickness increases.

Table 3.5. Fit parameters for SABC contacted to D_2O in the C-F region. A, x, and w are signal strength, peak center, and peak width respectively.

Thickness (nm)	24	35	65	78
NR	0	0	0	0.9
A1	-12	-12	-10	-10
x01	1375	1375	1372	1382
W1	8	8	8	8
A2	46	45	44	35
x02	1448	1455	1455	1448
W2	12	12	12	12

Table 3.6. A/Γ values for 1375 cm^{-1}.

Thickness (nm)	A/Γ Air	A/Γ D_2O
103	7.49	
78	10.13	2.92
65	8.93	3.66
35	9.40	3.74
24	6.52	3.83

The change in the observed results is much larger than the change in the Fresnel coefficients for either the polymer/D_2O interface or the CaF_2/polymer buried interface (Figure 3.13). There is only a 1-2% change in the Fresnel factors in the 24-80 nm thickness range for the polymer/D_2O interfaces. The buried interface experiences a slightly larger change with a ~5% difference between 24 nm and 80 nm, and a ~9% difference between the highest and lowest Fresnel coefficient in that range. Therefore, the C-F signal is likely a contribution from both interfaces. The overall signal intensities observed in air are much stronger than those in water, as shown in Figures 3.10 and 3.12. Even though the contribution from the polymer/substrate interface is the same in the two environments, it does not play a noticeable role in the signals observed in air, because the signal in air is dominating. For water, it will affect the observed overall signal because the signal from the polymer/water interface is weak.

The observation of the C-F stretching signal from the polymer/D_2O interface is surprising as it would be expected that the highly hydrophobic fluorinated groups would

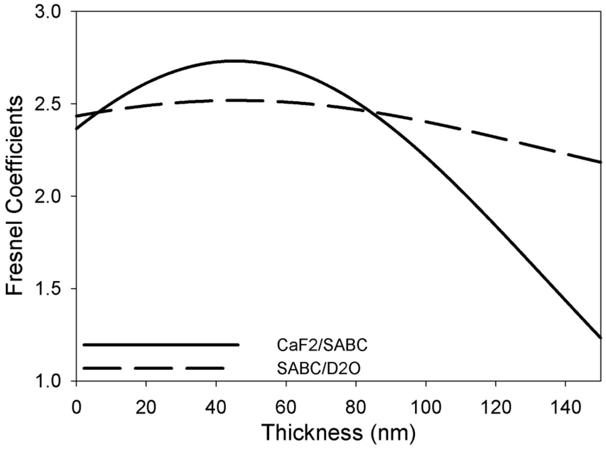

Figure 3.13. Fresnel coefficients as a function of thickness for the CaF_2/SABC interface and the SABC/D_2O interface at 1370 cm^{-1}.

not expose to water but bury themselves in the bulk polymer. The fluorinated portion is attached to the hydrophilic PEG portion, it is physically constrained to remain near the surface. As the hydrophilic PEG groups move to the surface for the more favorable interaction with the hydrophilic environment provided by the D_2O, the fluorinated portions are forced to stay on the surface. Hence, it is possible to detect these groups even though it would be unexpected that they would be present.

3.4 CONCLUSIONS

SFG has been used to examine the surface structures of a potential marine antifouling coating. This coating material contains hydrophobic fluoroalkyl groups as well as a hydrophilic PEG group. In air, the alkyl groups tend to stand more towards the surface normal, whereas when in contact to water they adopt a much larger angle to the surface normal to minimize unfavorable interactions with the D_2O. The fluorinated groups are seen at both the polymer/air and the polymer/D_2O cases. The fluorinated groups appear at the surface in air due to the hydrophobic interactions, while hydrophilic PEG portion is likely further from the surface. Upon contact with water the PEG migrates to the surface to interact with the water resulting in the increase of the SFG asymmetric methylene stretch signal. Surprisingly, despite the fact that the fluorinated groups are expected to retreat into the bulk in an aqueous environment, they are still detected at the surface. As the fluorinated groups are attached to the hydrophilic PEGylated portion of the polymer, they may be constrained to remain near the surface while the PEG optimizes its interaction in the hydrophilic D_2O environment.

The surface behavior of this polymer correlates well with anti-fouling testing results using *Ulva* spores and *Navicula* cells, two materials commonly used to test anti-fouling properties. *Ulva* is known to adhere strongly to hydrophilic surfaces, while *Navicula* is known to attach strongly to hydrophobic surfaces. Both *Ulva* and *Navicula* were shown to have high removal from the SABC, indicating that amphiphilic nature of the SABC.[10] The amphiphlic nature of the SABC surface in water is reflected in the observed SFG spectra as discussed above.

3.5 REFERENCES

(1) Weinman, C. J.; Finlay, J. A.; Park, D.; Paik, M. Y.; Krishnan, S.; Fletcher, B. R.; Callow, M. E.; Callow, J. A.; Handlin, D. L.; Willis, C. L.; Fischer, D. A.; Sohn, K. E.; Kramer, E. J.; Ober, C. K. *Polymeric Materials: Science & Engineering Preprints* **2008,** *98*, 639-640.

(2) Weinman, C. J.; Finlay, J. A.; Park, D.; Paik, M. Y.; Krishnan, S.; Sundaram, H. S.; Dimitriou, M.; Sohn, K. E.; Callow, M. E.; Callow, J. A.; Handlin, D. L.; Willis, C. L.; Kramer, E. J.; Ober, C. K. *Langmuir* **2009,** *25,* 12266-12274

(3) Krishnan, S.; Ayothi, R.; Hexemer, A.; Finlay, J. A.; Sohn, K. E.; Perry, R.; Ober, C. K.; Kramer, E. J.; Callow, M. E.; Callow, J. A.; Fischer, D. A. *Langmuir* **2006,** *22*, 5075-5086.

(4) Brady, R. F.; Singer, I. L. *Biofouling* **2000,** *15*, 73-81.

(5) Lu, X.; Shephard, N.; Han, J.; Xue, G.; Chen, Z. *Macromolecules* **2008**, *41*, 8770-8777.

(6) Lu, X.; Li, D.; Kristalyn, C.; Han, J.; Shephard, N.; Rhodes, S.; Xue, G.; Chen, Z. *Macromolecules* **2009**, *42*, 9052-9057

(7) Wang, J.; Chen, C.; Buck, S. M.; Chen, Z. *J. Phys. Chem. B*, **2001**, *105* 12118–12125.

(8) Wilk, D.; Johannsmann, D.; Stanners, C.; Shen, Y. R. *Phys. Rev. B* **1995**, *51*, 10057-10067.

(9) Feller, M. B.; Chen, W.; Shen, Y. R. *Phys. Rev. A* **1991**, *43*, 6778-6792.

(10) Shen, Y. R. *Annu. Rev. Phys. Chem.* **1989**, *40*, 327-350.

(11) Wang, J.; Paszti, Z.; Even, M. A.; Chen, Z. *J. Am. Chem. Soc.* **2002**, *124*, 7016–7023.

(12) Snyder, R. G.; Strauss H. L.; Elliger, C. A. *J. Phys. Chem.* **1982**, *86*, 5145-5150.

(13) Tyrode, E.; Johnson, C. M.; Rutland, M. W.; Day, J. P. R.; Bain, C. D. *J. Phys. Chem. C.* **2007**, *111*, 316-329.

(14) Lenk, T. J.; Hallmark, V. M.; Hoffman, C. L.; Rabolt, J. F.; Castner, D. G.; Erdelen, C.; Ringsdor, H. *Langmuir* **1994**, *10*, 4610-4617.

CHAPTER 4: INVESTIGATION OF SUB-MONOLAYER, MONOLAYER, AND MULTILAYER SELF-ASSEMBLED SEMIFLUORINATED ALKYLSILANE FILMS

4.1 INTRODUCTION

In the previous two chapters, polymer surfaces and interfaces were studied using SFG. Some of these polymers contain fluorinated functional groups. SFG data analysis for C-H stretching signals have been extensively investigated, however SFG signals on C-F stretching signals have been seldom investigated. In this chapter, SFG was applied to study a relatively simple self-assembled fluorinated thin layer. Self-assembled (SA) films, including self-assembled monolayers (SAMs), are potentially well-organized structures widely used as surface modification layers in biomedical, lubrication, (opto)electronic, lithographic, and numerous additional applications.[1-5] The utility of these materials for such applications arises from the ability to tailor film properties through molecular design of the precursor components. Chain-surface interactions can be tailored by varying the constituent molecules' head groups, through which the chains are attached to the surface via covalent or non-covalent interactions. Alternatively, changing the tail groups allows for the optimization of surface properties (e.g., hydrophobicity) or the introduction of functional groups as a prelude to further chemistry.[3,4]

Fluoroalkyl (FAS) SA films can be fabricated on oxide substrates, such as SiO_2, using an $F(CF_2)_n(CH_2)_mSiCl_3$ precursor to produce surfaces with relatively high thermal stability, low energy, and high hydro- and oleophobicity.[4] FAS SA films have been used in microelectromechanical systems (MEMS)[6,7] and as surface modification layers in organic electronic device applications,[8-11] which rely on the formation of well-defined, homogeneous structures.

Unlike their monofunctional counterparts (e.g., alkane thiols on Au), trifunctional silane precursors such as $F(CF_2)_n(CH_2)_mSiCl_3$ allow for the formation of highly crosslinked two- and possibly three-dimensional structures. An idealized mechanism of SAM formation from trifunctional precursors begins with the nucleation of small 'islands' of coverage, which gradually expand to fully cover the substrate. As coverage increases with deposition time, the van der Waals interactions between alkyl segments serve as a driving force that causes previously disordered chains lying down on the surface to become more ordered and to stand up at some tilt angle from the surface normal. A corresponding change is observed in surface-sensitive parameters, such as water contact angle.[2-5]

In this ideal system, the resultant structures would form well-defined networks, whereby each hydrolyzed silane molecule bonds to two adjacent molecules and to the substrate (Figure 4.1) in a well-controlled process ending in the formation of a uniform

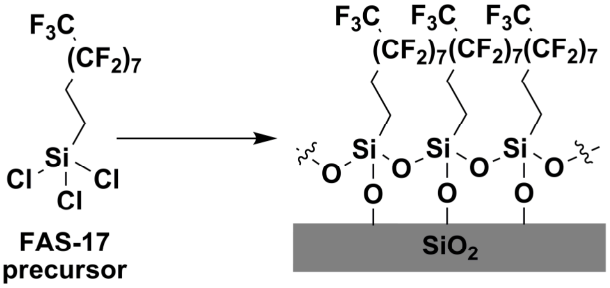

Figure 4.1. Formation of an idealized self-assembled monolayer from the FAS-17 precursor.

monolayer.[4] However, as the field has matured, it has become apparent that the complex and dynamic series of chemical and physical processes involved in SA film formation depends strongly on a myriad interconnected variables, including chemical functionality, substrate and solvent humidity, precursor concentration, deposition method, temperature, and deposition time.[2-4] Because the trifunctional $F(CF_2)_n(CH_2)_mSiCl_3$ precursor molecules are unlikely to universally bond in the 2:1 neighbor:substrate manner, it is more likely that a distribution of bonding patterns occurs. Thus, if even only a few molecules fail to follow the ideal pattern, those molecules may initiate the formation of one or more relatively localized additional layers. This would give rise to an inhomogeneous multilayer structure, such as the one shown in Figure 4.2C, and afford a distribution of thicknesses across the film. Such structures are particularly likely when precursor molecules react and aggregate in solution prior to adsorption; this has been shown to occur under various fabrication conditions.[2-4] It is reasonable that the presence of the long, electron-withdrawing FAS chain significantly increases this likelihood by increasing the reactivity of the Si reaction center; indeed, Bunker et al. observed the formation of aggregates in solutions of FAS-17.[5]

As a result of this added complexity, the effects of fabrication conditions, including deposition time, on formation mechanisms and resultant molecular architectures of these trifunctional systems are less well understood compared to those of their monofunctional counterparts. A number of techniques, including solution[9-10,12,13] and vapor[6,14] deposition have been used to fabricate FAS SA films. However, since these films are often fabricated as one component of a multi-step, application-driven procedure, the resultant films are often assumed to be ideal monolayers and used without further

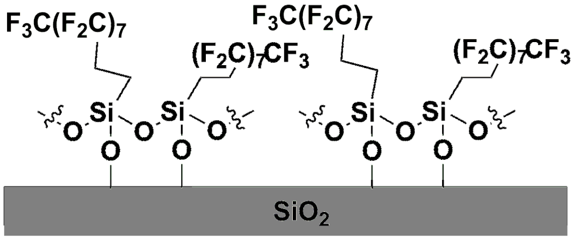

(A) 2sFAS-17

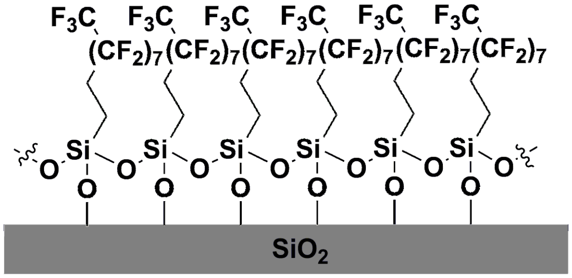

(B) 5mFAS-17

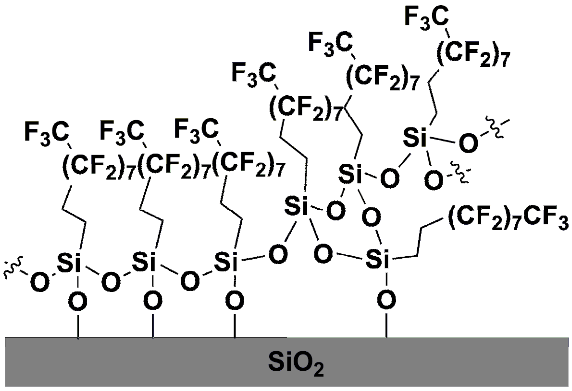

(C) 20mFAS-17

Figure 4.2. Self-assembled film coverage as a function of deposition time: (A) less-ordered sub-monolayer coverage at short deposition times (2sFAS-17); (B) well-ordered monolayer coverage at intermediate deposition times (5mFAS-17); (C) slightly-disordered multilayer coverage at long deposition times (20mFAS-17). Note that -O-Si-O- bonding is idealized for simplicity.

structural verification; see ref. 3 for thorough discussion.[3] Previous work has demonstrated that the supramolecular structure, orientation, and surface properties depend on myriad fabrication parameters.[2-4] Thus, it is necessary to gain a better understanding of FAS SA film formation and properties by combining surface-sensitive and bulk characterization techniques.

Sum frequency generation (SFG) spectroscopy is a second-order nonlinear technique that has proven to be a powerful tool in surface characterization. SFG has been used to examine mixed SAMs consisting of binary combinations of alkyl- and fluoro-octyltrichlorosilanes.[12,13,15] It was observed that in these mixed monolayers, peak centers of some vibrational modes shift, compared to those in the pure component, due to the adsorption of both species on the substrate. This gives rise to SFG spectra with complexity beyond merely a linear combination of the two component species. Even though these studies involved fluorinated molecules, only SFG C-H stretching signals were examined.

Very few studies have been conducted using SFG spectroscopy in the C-F stretching frequency region. SFG spectra of polytetrafluoroethylene (PTFE) were collected by Ji et al.[16] By shearing PTFE at 300°C against a fused silica substrate, these researchers were able to observe the E_1 symmetry vibrational modes at 1142 and 1204 cm^{-1} along the shear direction on the PTFE surface. The C-F stretching SFG signal from the CF_3 group of 4-(trifluoromethyl)benzyl alcohol, which arises from the strong coupling between the C-F stretching modes and the stretching and bending modes of the adjacent aromatic ring, was also detected.[17] More recently, Tyrode et al.[18] observed SFG signals at 1369, 1408, and 1665 cm^{-1} from ammonium perfluorononanoate (APFN) in a water solution at the air-liquid interface. The 1369 cm^{-1} peak was assigned to the CF_3 stretching mode, while those at 1408 and 1665 cm^{-1} were assigned to carboxylate stretch vibrations.

In this study, FAS-17 SA films were prepared from an $F(CF_2)_8(CH_2)_2SiCl_3$ precursor via solution deposition using various deposition times (2 s, 5 min, and 20 min). These samples will be referred to as 2sFAS-17, 5mFAS-17, 20mFAS-17. A suite of surface-sensitive and bulk analytical techniques were combined to examine the effects of these deposition times on the supramolecular organization and surface properties of the resultant SA films. Surface hydrophobicity was characterized by contact angle goniometry. SFG spectroscopy was utilized to examine differences in surface coverage and chain orientation. Fourier-transform infrared spectroscopy (FTIR) was used to verify C-F SFG peak assignments. X-ray photoelectron spectroscopy (XPS) confirmed precursor reaction and afforded information about relative surface coverage. SA film thicknesses were determined by ellipsometry.

Our contact angle, SFG, XPS, and ellipsometry results are consistent with the formation of disordered sub-monolayer structures at short deposition times, well-ordered monolayers at intermediate deposition times, and inhomogeneous multilayers at long deposition times. Based on SFG results and underlying group theory as well as the observation of similar signals in the FTIR spectrum of a $CF_3(CH_2)_2SiCl_3$ sample—in which CF_3 groups are the only fluorinated moieties—allowing for the assignment of the SFG signals to the asymmetric stretch of the FAS-17 chain's terminal CF_3 group. While this assignment contrasts with the more commonly-invoked CF_2 axial stretching assignment, it is supported by the recent observations of Tyrode et al.[18] These SFG signals, which are the first reported in the C-F stretching frequency region for FAS SA films, were used to confirm a difference in semifluorinated silane chain orientation between the disordered sub-monolayer and well-ordered monolayer samples.

4.1 EXPERIMENTAL

4.2.1 Sample Preparation

Fused silica windows (IR grade, Esco) were freshly cleaned before use via glow discharge plasma treatment, overnight immersion in chromic acid, rinsing with Millipore water, and drying under N_2. FAS-17 ($F(CF_2)_8(CH_2)_2SiCl_3$, Gelest), FAS-3 ($CF_3(CH_2)_2SiCl_3$, Gelest) anhydrous hexadecane (Aldrich), and anhydrous $CHCl_3$ (Aldrich) were used as received.

FAS-17 SA films were fabricated from the $F(CF_2)_8(CH_2)_2SiCl_3$ precursor on freshly cleaned fused silica windows via solution deposition in a moderate humidity environment under otherwise ambient conditions. Substrates were cleaned just prior to fabrication to afford a pristine native oxide layer. A humidity chamber was devised by placing open containers of $MgNO_3 \cdot 6\,H_2O$ (sat., aq.) in the bottom of a dessicator to control the substrate hydration and afford a relatively consistent humidity level (48% ± 4%, depending on ambient temperature).[19] Prior to modification, the freshly cleaned windows were stored in a jar in this chamber. In the same humidity chamber, the windows were then immersed in a separate jar containing a solution of FAS-17 (48 mg, 2.0 mM) in 4:1 hexadecane:$CHCl_3$ (40 mL total) for either 2 s, 5 min, or 20 min. A number of previous procedures have included CCl_4 in the FAS-17 solvent system. As substituting $CHCl_3$ had no significant effect on the resultant SA films, it was elected to use it as a less-toxic alternative to CCl_4. The samples were then immediately rinsed in fresh $CHCl_3$ three times under sonication to remove any unreacted FAS precursor, dried under N_2, and annealed at 100 °C for 1 h. Based on contact angle measurements (not shown), it was found that thermal annealing was necessary to erase any metastable states established during fabrication and to optimize chain packing. Samples were stored under ambient conditions.

4.2.2 Contact Angle

Water contact angle can be used to characterize the surface hydrophobicity of a material. Static water (18.2 MΩ Millipore) contact angle measurements were obtained using a KSV CAM 100 Optical Contact Angle Meter. An average of the left and right contact angles was calculated for each of ten captured frames per water drop; each sample was examined in five or more areas per experiment. Multiple samples were examined for each deposition time, and contact angle experiments were repeated periodically. Statistical analysis was used to evaluate consistency between individual measurements, between samples made under the same conditions, and between replicate contact angle experiments. Measurements were considered outliers only when it was clearly demonstrated that they fell outside two standard deviations from the mean (95% confidence level). Each reported contact angle value reflects the average of at least 100 individual measurements.

4.2.3 Ellipsometry

Thickness measurements were obtained using a Nanofilm Surface Analysis EP3-SW single wavelength imaging ellipsometer (Nanofilm Technologies) with EP3View software (λ = 532 nm, angle of incidence = 60°, k = 0.01, η (SiO_2) = 1.46). FAS-17 SA film thicknesses were calculated using a refractive index of 1.33.[20] Each reported value is the average of at least 18 measurements obtained from several samples.

4.2.4 XPS

X-ray photoelectron spectroscopy is an ultra-high vacuum, surface-sensitive technique used to analyze the surface chemistry (e.g., surface elemental composition, chemical state, and electronic state) of a material. Here, XPS spectra were acquired using a Kratos Axis Ultra DLD with a monochromatic Al source and 0.1 eV step size. The peaks in the experimental spectra were fitted and referenced to the CC/CH peak centered at 285 eV. Spectra were analyzed using CasaXPS software with line shapes consisting of 70% Gaussian and 30% Lorentzian functions.

4.2.5 SFG

The underlying SFG theory has been described in detail in Chapter 1. The experiments described herein utilize a face-up sample geometry (Figure 1.3B), where the frequency-fixed visible beam overlaps with the frequency-tunable infrared beam on the SA film formed on the top face of a fused silica window. SFG spectra were collected in the ssp (s polarized sum, s polarized visible, p polarized IR), ppp, and sps polarization combinations.

4.2.6 FTIR

FTIR experiments were carried out using a Nicolet Magna 550 FTIR spectrometer. A few drops of FAS-3 were placed in a Harrick demountable liquid cell (Pleasantville, NY) made of CaF_2 windows (25 mm by 2 mm). The reported spectrum is an average of 32 scans from 1300 to 1400 cm^{-1} range.

4.3. RESULTS AND DISCUSSION

4.3.1 Contact angle measurements

Average contact angle measurements for the FAS-17 SA films are shown in Table 4.1. For each deposition time used, a data set was compiled that included all of the contact angle measurements obtained for samples fabricated using that deposition time. The data reported in Table 4.1 represent the mean and standard deviation values calculated from these data sets.

Table 4.1. Contact angle measurements, thickness measurements, and XPS $C\underline{F}_x:\underline{Si}O_y$ peak area ratios for FAS-17 self-assembled films.

Sample	Contact Angle	Thickness (nm)	Ratio of $C\underline{F}_x:\underline{Si}O_y$
20mFAS-17	109.7 ± 2.7°	3.1 ± 1.2	14.2
5mFAS-17	111.2 ± 2.3°	1.4 ± 0.4	6.42
2sFAS-17	88.8 ± 2.1°	< 1	1.74

Clean, unmodified fused silica windows exhibit static water contact angles below 10º, as expected of a hydrophilic surface. The 2sFAS-17 samples afford average contact angles of approximately 89º, while the 5mFAS-17 and 20mFAS-17 samples display average contact angles of approximately 110º and 111º, respectively. The latter two values are statistically identical and reasonable for a highly fluorinated surface.[21]

Static water contact angles are a measure of macroscale surface hydrophobicity, which is related to the surface coverage (i.e., number of molecules adsorbed on a surface) as well as the relative polarity, orientation, and degree of ordering (i.e., the distribution of different molecular orientations) of these adsorbed molecules. Contact angles for highly fluorinated surfaces are known to exceed 100º.[21] Thus, the significantly lower average contact angle obtained for the 2sFAS-17 samples clearly indicates reduced coverage and/or ordering, in comparison to the samples fabricated from longer deposition times.

As contact angle measurements alone are not sufficient to determine the individual effects of coverage and ordering, it was necessary to perform additional studies using other analytical techniques, such as XPS, SFG, and ellipsometry.

4.3.2 Ellipsometry studies

The effect of deposition time on resultant layer thickness was examined by ellipsometry, whereby a change in the polarization of light as it travels through a medium is measured and used to calculate layer thickness of that medium. A SAM comprised of all-trans, fully-extended FAS-17 molecules oriented normal to the surface would have a thickness of 1.6 nm. The thickness of an FAS-17 SAM has been measured to be 1.34 nm,[11] which is in agreement with the thickness expected given the tilt from surface normal expected in these systems.

Average measured thicknesses for the 2sFAS-17, 5mFAS-17, and 20mFAS-17 SA films are given in Table 4.1. Thickness measurements for samples fabricated with short deposition times (2sFAS-17) proved challenging to obtain, indicating that these samples are most likely less than 1 nm thick. Such measurements are consistent with incomplete surface coverage by the FAS-17 molecules (Figure 4.2A), as discussed in previous sections. Samples fabricated with intermediate deposition times (5mFAS-17) have an average thickness of 1.42 nm, which is in close agreement with literature measurements for monolayer coverage.[11] This result is consistent with an extended chain conformation tilted approximately 29° from the surface normal; such behavior is reasonable for a SAM comprised of C_{10} chains (Figure 4.2B).[11] In contrast, SA films fabricated with long deposition times (20mFAS-17) exhibit an average thickness of 3.10 nm, with a sizable standard deviation of 1.22 nm. These results are two to three times greater than expected for an ideal monolayer and are in line with the formation of an inhomogeneous multilayer (Figure 4.2C).[5]

4.3.3 XPS studies

XPS experiments were carried out to study the relative surface coverage of FAS-17 SA films as a function of deposition time and were correlated with the results obtained from contact angle, SFG, and ellipsometry studies. The lack of signal in the Cl 2p characteristic region, 190-200 eV, of the survey spectrum of each sample (Figure 4.3) indicates that no FAS-17 precursor remained after fabrication. Core spectra in the C 1s, F 1s, and Si 2p regions (Figure 4.4) were obtained for each FAS-17 sample. The C 1s peak fitting results correlate with the presence of five chemically different carbons: $\underline{C}F_3$ (294.1 eV), $\underline{C}F_2CF_2$ (291.9 eV), $\underline{C}F_2CH_2$ (291.0 eV), $\underline{C}H_2CF_2$ (286.4 eV), and $\underline{C}H_2CH_2$ (285.0 eV).[22]

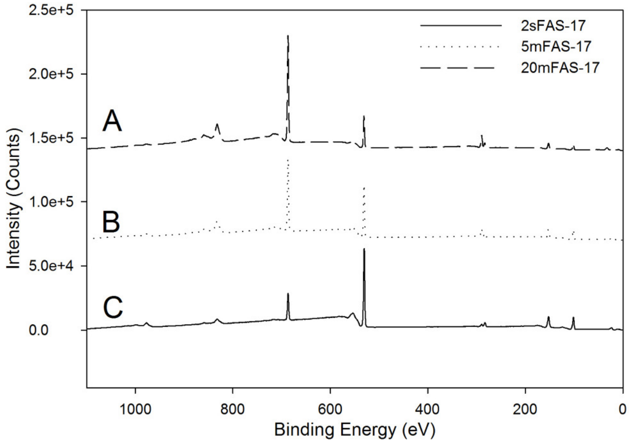

Figure 4.3. XPS survey spectra of FAS-17 self-assembled films: (A) 20mFAS-17, (B) 5mFAS-17, (C) 2sFAS-17. Absence of Cl 2p peak at 190-200 eV indicates a complete reaction of the FAS-17 precursor.

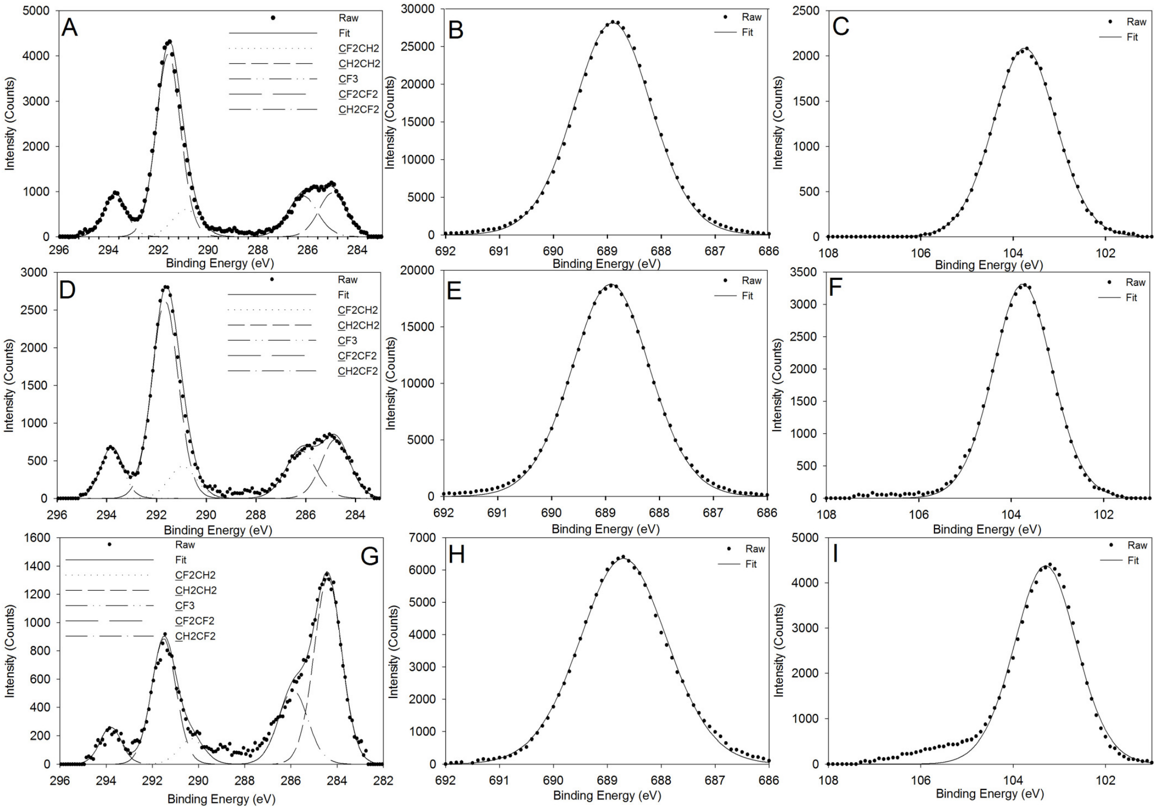

Figure 4.4. XPS core spectra of FAS-17 self-assembled films: (A) 20mFAS-17 C 1s region, (B) 20mFAS-17 F 1s region, (C) 20mFAS-17 Si 2p region, (D) 5mFAS-17 C 1s region, (E) 5mFAS-17 F 1s region, (F) 5mFAS-17 Si 2p region, (G) 2sFAS-17 C 1s region, (H) 2sFAS-17 F 1s region, (I) 2sFAS-17 Si 2p region. Symbols represent experimental data, solid lines show the best fit, and varied dashed lines comprise component peaks in the C 1s region attributed to $\underline{C}F_3$, $\underline{C}F_2CF_2$, $\underline{C}F_2CH_2$, $\underline{C}H_2CF_2$, and $\underline{C}H_2CH_2$.

As XPS can be used to measure the relative adsorption of molecular species on a surface, the ratio between given XPS peak areas can be used to make relative comparisons regarding substrate coverage (i.e., number of silane chains adsorbed) as a function of deposition time. Table 4.2 displays 20mFAS-17 : 5mFAS-17 and 5mFAS-17 : 2sFAS-17 peak area ratios for each type of chemically different fluorocarbon observed. The 5mFAS-17 : 2sFAS-17 and 20mFAS-17 : 5mFAS-17 peak area ratios for the $\underline{C}F_3$, $\underline{C}F_2CF_2$, and $\underline{C}F_2CH_2$ species are all greater than unity, correlating to an increase in the number density of fluorinated material adsorbed as a function of deposition time.

Table 4.2. XPS peak area ratios for $\underline{C}F_3$, $\underline{C}F_2CF_2$, and $\underline{C}F_2CH_2$.

	Peak area ratios		
	$\underline{C}F_3$	$\underline{C}F_2CF_2$	$\underline{C}F_2CH_2$
20mFAS-17 : 5mFAS-17	1.42	1.42	1.42
5mFAS-17 : 2sFAS-17	2.50	2.94	2.38

However, the ratios are larger for 5mFAS-17 : 2sFAS-17 than for 20mFAS-17 : 5mFAS-17, indicating that the rate of adsorption decreases with time but remains non-zero.

In comparison to the C 1s spectral region, peak assignments for the F 1s and Si 2p core spectra are slightly more straightforward, as each region contains fewer chemically distinct species. The F 1s peak (689.1 eV) originates from the carbon-bound fluorine, $C\underline{F}_x$.[23] It can be seen to increase significantly as deposition time increases, likely due to increased adsorption of fluorinated silane chains. Two potential $\underline{Si}O_y$ species contribute to the Si 2p region (103.9 eV): the $\underline{Si}O_2$ substrate and the $-CH_2-\underline{Si}-O_3-$ moieties that comprise the SA network.[23] If the Si 2p peak arises from the SA network, the $\underline{Si}O_y$ peak would increase in intensity, as more FAS-17 material is adsorbed with time. However, the $\underline{Si}O_y$ peak intensity decreases with deposition time (Figure 4.4), indicating that at least the majority of the $\underline{Si}O_y$ peak arises from the substrate.

Comparison of the XPS $C\underline{F}_x$ and $\underline{Si}O_y$ peak area ratios (Table 4.1) allows for the evaluation of relative FAS-17 SA film surface coverage. According to the idealized mechanism of SAM formation discussed above, the adsorption of FAS-17 molecules on the fused silica substrate surface should increase over time before leveling off with the formation of a full monolayer.[22] This trend would be reflected in the resultant XPS peak areas, which are proportional to the number density of the characteristic chemical species sampled. As a single FAS-17 unit comprises 17 F atoms for each Si atom, the corresponding $C\underline{F}_x$ signal area should increase more rapidly than that of the $\underline{Si}O_y$ signal as the FAS-17 chains adsorb on the substrate. In this idealized monolayer mechanism, this increase would continue until a monolayer is formed, at which time the signal would remain constant. Thus, the ratio of $C\underline{F}_x$ to $\underline{Si}O_y$ peak areas would also increase before becoming constant at full monolayer coverage.

The $C\underline{F}_x$ to $\underline{Si}O_y$ signal ratios for FAS-17 SA films (Table 4.1) increased with deposition time but did not reach a constant value, even as the corresponding contact angles leveled off. For 2sFAS-17 samples, an $C\underline{F}_x$ to $\underline{Si}O_y$ ratio of 1.74 indicates a low degree of coverage in agreement with the observed, relatively low contact angle (89º). The ratio increases to 6.42 for 5mFAS-17 samples, which is also consistent with the higher contact angle (111º) of a highly fluorinated surface. While increasing the deposition time to 20 min does not drastically change the resultant contact angle (110º), the $C\underline{F}_x$ to $\underline{Si}O_y$ ratio increases significantly to 14.2. This suggests that additional adsorption continues at longer deposition times, even though intermediate deposition times seem to be sufficient to impart the macroscopic properties (i.e., hydrophobicity) of at least a nearly passivated surface.

4.3.4 SFG studies

SFG signal intensity, which arises from the vibrational mode of a given functional group, can be influenced by both the surface coverage and surface orientation of the functional group. If the surface coverage is known, surface orientation can be deduced from the SFG signal intensity.[24] In the above discussion, it was shown that XPS can be used to determine relative surface coverage for FAS SA film samples prepared using different deposition times. SFG can be used to compare the orientation of FAS molecules in different samples. Previous studies of semifluorinated SAMs have been restricted to the C-H stretching frequency region and have examined the interactions between mixtures of semifluorinated silane and the analogous alkyl silane chains in binary mixtures.[12,13,15] The C-H stretching region of our FAS-17 SA films were briefly examined and it was found that our results are in agreement with those presented by Lagutchev et al.[12,13,15] In this chapter, a discussion of the C-F stretches of the FAS-17 SA films will be the focus.

C-F peak assignment. SFG spectra of FAS SA films were obtained at the film-air interface in the C-F stretching spectral region using ssp and ppp polarization combinations (Figure 4.5). No discernable SFG signal is detected between 1300 and 1400

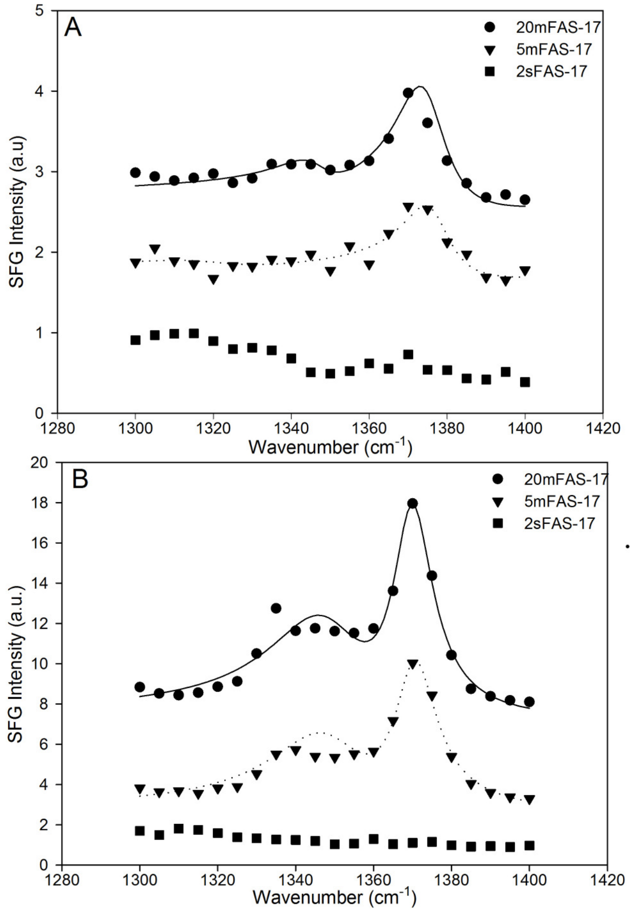

Figure 4.5. SFG spectra for FAS-17 self-assembled films in the (A) ssp polarization and (B) ppp polarization combinations. Symbols represent experimental data, and lines represent the best fit.

cm^{-1} from the 2sFAS-17 samples. The spectra can be fitted with two peaks (~1345 and ~1370 cm^{-1}) in the C-F stretching region for the 5mFAS-17 and 20mFAS-17 samples. None of the samples examined give rise to detectable signals in the sps polarization combination in the C-F stretching frequency region.

Upon reviewing various reports in the literature,[18,25] it became clear that the peak assignments for the ~1345 and ~1370 cm^{-1} peaks are the subject of some debate. In the SAMs community, these two peaks have typically been assigned to vibrational modes of CF_2 backbones, based on observations by Lenk et al.[25] It has been repeatedly reported that the peaks in the 1320-1380 cm^{-1} region result from the strong symmetric CF_2 stretching component along the fluorinated backbone axis; consequently, stretches in this region have been commonly referred to as axial CF_2 stretches. However, Tyrode et al. propose a different assignment, based on their recent SFG study of ammonium perfluorononanoate (APFN).[18] These researchers also observed two peaks in the 1320-1380 cm^{-1} region. However, changing the terminal CF_3 group to CF_2H results in the loss of SFG signal in this region, suggesting that these SFG signals arise from CF_3 groups. In addition, concentration and polarization dependence were each observed for both the 1330 and 1369 cm^{-1} peaks simultaneously. Based on these observations, Tyrode and coworkers assigned both the 1330 and 1369 cm^{-1} signals to the nondegenerate asymmetric CF_3 stretches.[18]

Group theory allows for validation of these peak assignments. Given that molecules in fluorinated SA films are widely believed to adopt a helical structure,[26] the FAS molecule in our system can be treated as a helix composed of 7 CF_2 units angularly separated by 168 degrees from each other. This helix can be considered to possess the

D(14Π/15) point group symmetry[26] and have the identical irreducible representations with the D_5 point group. In general, the orientation of such helices can be determined using the similar SFG orientation analysis methodology that has been developed and applied to helical structures.[27-30] However, in the case of structures with D_5 symmetry, only the E_1 mode is both IR and Raman active. As only vibrational modes that are both IR and Raman active can be observed by SFG, only the E_1 mode in the FAS system is SFG-active. Based on this symmetry argument, the E_1 mode for the point group D_5 can only be probed by SFG in the sps polarization combination.[16] Thus, SFG signal corresponding to axial CF_2 stretching would be observable in the sps polarization combination; in such a scenario, no SFG signal would be observable in the ssp and ppp combinations.

None of our FAS SA films give rise to SFG signal in the sps polarization combination. In contrast, SFG signals at approximately 1345 and 1370 cm^{-1} in both the ssp and ppp polarization combinations were detected, as stated earlier. Therefore, we believe that the SFG signals obtained in the 1300-1400 cm^{-1} frequency region from FAS SA films are unlikely to arise from the CF_2 backbone.

As discussed above, Tyrode and coworkers proposed that the SFG peaks between 1300 and 1400 cm^{-1} arise from the terminal CF_3 asymmetric stretching modes of fluorinated molecules, based on C_s symmetry.[18] In this C_s symmetry case, the SFG susceptibility components suggest a constant χ_{yyz}/χ_{zzz} SFG signal ratio independent of the tilt angle, θ.[26-28] Therefore, calculation of θ and, consequently, the orientation of the CF_3 terminal group, are not possible using the measured SFG signal in the ssp and ppp polarization combinations. In our system, the measured signal strength ratios are not identical for the 5mFAS-17 and 20mFAS-17 spectra in the ssp and ppp polarization combinations. It is possible that C_s symmetry may be an imprecise model for the CF_3 groups in this case.

An FTIR spectrum of $CF_3(CH_2)_2SiCl_3$ (FAS-3) was obtained (Figure 4.6) to further verify the ~1345 and ~1370 cm^{-1} peak assignments. Two peaks, at 1320 and 1374 cm^{-1}, are observed. As the terminal CF_3 group is the only fluorinated moiety in the molecule, it is likely that the two FTIR peaks observed between 1300 and 1400 cm^{-1} originate from that functional group. Thus, the FTIR result supports the assignment of the ~1345 and ~1370 cm^{-1} signals to the CF_3 asymmetric stretches.

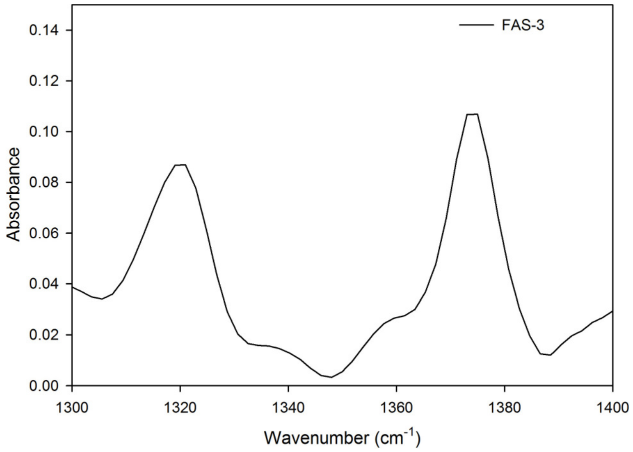

Figure 4.6. FTIR spectrum of FAS-3. The peaks at 1320 and 1374 cm^{-1} are assigned to the asymmetric stretching of the CF_3 group.

Comparison of orientation. As discussed in the previous section, the 2sFAS-17 samples produce no SFG signal, a result consistent with at least one of two cases: poor surface coverage and/or essentially random orientation of the silane molecules. Either case would suggest the absence of a full, well-ordered self-assembled monolayer. This indication is further supported by contact angle, XPS, and ellipsometry results.

Decoupling the effects of coverage and orientation requires correlation with XPS results and is discussed below.

The SFG spectral fitting results for 5mFAS-17 and 20mFAS-17 films in both the ssp and ppp polarization combinations are listed in Table 4.3. The ~1345 and ~1370 cm^{-1} signals are assumed to arise from asymmetric stretching modes of CF_3 with C_s symmetry, as described above. Thus, information about the orientation of CF_3 groups on the surface cannot be derived from our measured ppp/ssp signal strength ratio, as that ratio is not sensitive to the FAS chain orientation. For this reason, no orientation analyses for the 5mFAS-17 and 20mFAS-17 samples are discussed herein.

Table 4.3. SFG fit parameters for spectra of FAS-17 self-assembled films. A, x, and w are signal strength, peak center, and peak width, respectively.

Sample	5 min ssp	20 min ssp	5 min ppp	20 min ppp
NR	-0.31	-0.36	-0.21	-0.31
A1	1.7	1.7	23.7	26.6
x01	1320	1347	1349	1349
w1	15.0	7.0	15.0	15.0
A2	6.5	9.1	14.2	16.1
x02	1377	1375	1370	1370
w2	7. 6	8.0	6.6	6.2

However, based on the relative SFG signal strength and XPS peak areas, it is feasible to compare semifluorinated silane chain orientation between the 2sFAS-17 and 5mFAS-17 samples. If the orientation is assumed to be constant for all deposition times, then XPS intensity would be solely a function of coverage (number density). XPS peak areas corresponding to the CF_3 species can then be used to obtain a proportionality factor, K, which in turn can be used to predict the relative SFG signal intensity for the 2sFAS-17 samples. As SFG signal intensity is proportional to the square of number density, we can develop the relationship:

$$\text{SFG Intensity} = K \times (\underline{C}F_3 \text{ XPS Peak Area})^2 \qquad (4.1)$$

for each polarization combination. When calculated using the XPS peak areas from the 5mFAS-17 sample, $K_{ssp} = 1.17 \times 10^{-6}$ and $K_{ppp} = 9.99 \times 10^{-6}$. Using these values of K and the 2sFAS-17 $\underline{C}F_3$ peak area, the calculated ssp SFG intensity should be 0.11, which is well below our noise threshold of 0.3. However, the calculated ppp SFG intensity (0.96) would be detectable. As no ppp SFG signal is observed for the 2sFAS-17 sample, the 2sFAS-17 sample orientation must differ from that of the 5mFAS-17 sample.

The previously discussed contact angle, ellipsometry, and XPS results suggest increased coverage as a function of deposition time. SFG results also confirm that deposition time affects the formation of FAS SA films. Lack of SFG signal for 2sFAS-17 samples indicates that both orientation is different for low-coverage than for high-coverage surfaces. At longer deposition times, however, SFG signals are more sensitive to the deposition of additional FAS chains than to any potential changes in the underlying orientation because SFG spectroscopy is primarily surface-sensitive.

4.3.5 Further Discussion

The SFG signal intensity and contact angle values for the FAS SA films each correlate well as a function of deposition time. As CF_2 and CF_3 groups of fluoroalkyl silanes have been shown to give rise to different contact angles.[21] Contact angle measurements can be used to gain insight into the orientation of the semifluorinated silane chain at the surface. At shorter (2 s) deposition times, the average contact angle is significantly lower than that of samples fabricated using the intermediate (5 min) and long (20 min) deposition times, which do not vary significantly. The lower contact angle for the 2sFAS-17 samples supports the conclusion derived from the SFG data: the silanes have formed a disordered, sub-monolayer structure rather than a full, well-ordered SAM. It is probable that most of the silane chains are laying down on the surface, thereby displaying primarily CF_2 groups, which are less hydrophobic and result in smaller contact angles. In addition, the surface is covered by fewer silane chains than are surfaces exposed to the FAS-17 precursor for longer deposition times. The 5mFAS-17 and 20mFAS-17 samples exhibit contact angles consistent with a relatively well-ordered SA film, the surface of which is dominated by the terminal CF_3 groups.

SFG and contact angle data indicate that the 5mFAS-17and 20mFAS-17 samples are likely to be more similar to each other than either is to the 2sFAS-17 samples. This is consistent with the idealized SAM formation mechanism described above: coverage—and, consequently, contact angle and SFG signal intensity—increases quickly at early times, then gradually levels off. Based on this mechanism and the observed higher SFG signal intensity, it could be inferred that 20mFAS-17 samples would most likely correspond to 'better' SAMs than would the 5mFAS-17 samples. However, interesting trends arose during further exploration of these systems by XPS and ellipsometry, suggesting the formation of inhomogeneous silane multilayers at the longer (20 min) deposition times. Ellipsometry indicates that the measured thickness values for 2sFAS-17 samples correspond to sub-monolayer coverage, while the longest deposition time affords 20mFAS-17 samples with thicknesses up to 2-3 times greater than that expected for a monolayer. Only the 5mFAS-17 samples afford average thickness values (1.42 nm) in the expected 1.34 to 1.6 nm range. This is consistent with an extended conformation tilted approximately 29° from the surface normal; such behavior is reasonable for a SAM comprised of C_{10} chains.[11]

Combining the results from all four characterization techniques contributes to an understanding of the FAS self-assembly mechanism as a function of time. At short deposition times (2 s), the silane behaves in the expected fashion, with low coverage allowing most of the disordered molecules to lay parallel to the surface.[31] This results in relatively low contact angles, sub-monolayer thicknesses, and lower XPS peak intensities. The lower coverage and overall disorder preclude observation of SFG signal. As the deposition time increases to 5 min, additional silane surface coverage results in increased van der Waals interactions between the silane chains, giving rise to a well-ordered monolayer tilted approximately 29° from the surface normal. This conclusion is consistent with the observed contact angles, thickness measurements, increase in XPS $C\underline{F_x}$ to $\underline{Si}O_y$ peak area ratios, and SFG signals arising from the asymmetric stretches of the terminal CF_3 group. At longer deposition times (20 min), the thickness measurements obtained by ellipsometry and increased XPS signal intensities are consistent with the formation of inhomogeneous multilayers. Smaller changes in contact angle and SFG results are observed because these surface-sensitive techniques are less affected by the presence of multilayers.

4.4 CONCLUSIONS

Using a relatively simple method, semifluorinated SA films with sub-monolayer, monolayer, and multilayer surface coverage by varying the deposition times were prepared. A suite of surface-sensitive and bulk analytical techniques have been used to evaluate the coverage and relative orientation of these SA films. Contact angle and SFG intensity results alone can be considered consistent with an idealized mechanism of FAS SAM behavior for samples with 5 min and 20 min deposition times. However, when considered in light of ellipsometry, XPS, and further SFG analyses, a very different picture emerges. In films fabricated using long deposition times, FAS-17 forms inhomogeneous multilayers, which result in only a slight increase in SFG signal but a substantial increase in F 1s XPS peak intensity and measured film thickness. By correlating SFG and XPS results, it was demonstrated that there is a change in FAS-17 chain orientation as the deposition time increases from 2 s to 5 min. SFG and FTIR studies also afford additional evidence in support of the assignment of the ~1345 and ~1370 cm^{-1} vibrational modes to the asymmetric stretching modes of the semifluorinated silane chain's terminal CF_3 group rather than to its axial CF_2 stretches. To our knowledge, this is the first report of SFG spectra obtained for semifluoroalkyl silane self-assembled films in the C-F stretching frequency region.

In this chapter, a number of complimentary characterization techniques to investigate the impact of deposition time on the formation and surface properties of films self-assembled from fluorinated precursors were combined. Using this method, future work may focus on further refinement of the effect of deposition time or myriad other deposition parameters (e.g., water content, temperature, and solvent quality) on these and other supramolecular systems.

4.5 REFERENCES

(1) Sagiv, J. *J. Am. Chem. Soc.* **1980**, *102*, 92-98.

(2) Ducéré, J.-M.; Estève, A.; Dkhissi, A.; Rouhani, M. D.; Landa, G. *J. Phys. Chem. C* **2009**, *113*, 15652-15657, and references contained therein.

(3) Wen, K.; Maoz, R.; Cohen, H.; Sagiv, J.; Gibaud, A.; Desert, A.; Ocko, B. M. *ACS Nano* **2008**, *2*, 579-599, and references contained therein.

(4) Onclin, S.; Ravoo, B. J.; Reinhoudt, D. N. *Angew. Chem., Int. Ed.* **2005**, *44*, 6282-6304, and references contained therein.

(5) Bunker, B. C.; Carpick, R. W.; Assink, R. A.; Thomas, M. L.; Hankins, M. G.; Voigt, J. A.; Sipola, D.; de Boer, M. P.; Gulley, G. L. *Langmuir* **2000**, *16*, 7742-7751, and references contained therein.

(6) Knieling, T.; Lang, W.; Benecke, W. *Sens. Actuators, B* **2007**, *126*, 13-17.

(7) Maboudian, R.; Howe, R. T. *J. Vac. Sci. Technol.,B.: Microelectron, Nanometer Struct – Process., Meas., Phenom.* **1997**, *15*, 1-20, and references contained therein.

(8) Rhee, J.; Lee, H. H. *Appl. Phys. Lett.* **2002**, *81*, 4165-4167.

(9) Pernstich, K. P.; Goldmann, C.; Krellner, C.; Oberhoff, D.; Gundlach, D. J.; Batlogg, B. *Synth. Met.* **2004**, *146*, 325-328.

(10) Pernstich, K. P.; Haas, S.; Oberhoff, D.; Goldmann, C.; Gundlach, D. J.; Batlogg, B.; Rashida, A. N.; Schitter, G. *J. Appl. Phys.* **2004**, *96*, 6431-6438.

(11) Huang, C.; Katz, H. E.; West, J. E. *Langmuir* **2007**, *23*, 13223-13231.

(12) Lagutchev, A. S.; Song, K. J.; Huang, J. Y.; Yang, P. K.; Chuang, T. J. *Surf. Coat. Technol.* **1997**, *94-95*, 383-389.

(13) Huang, J. Y.; Song, K. J.; Lagoutchev, A. S.; Yang, P. K.; Chuang, T. J. *Langmuir* **1997**, *13*, 58-64.

(14) Tate, J.; Rogers, J. A.; Jones, C. D. W.; Vyas, B.; Murphy, D.W.; Li, W.; Bao, Z.; Slusher, R. E.; Dodabalapur, A.; Katz, H. E. *Langmuir* **2000**, *16*, 6054-6060.

(15) Lagutchev, A. S.; Song, K. J.; Huang, J. Y.; Yang, P. K.; Chuang, T. J. *Chem. Phys.* **1998**, *226*, 337-349.

(16) Ji, N.; Ostroverkhov, V.; Lagungné-Labarthet, F.; Shen, Y. R. *J. Am. Chem. Soc.* **2003**, *125*, 14218-14219.

(17) Even, M. A.; Lee, S. H.; Wang, J.; Chen, Z. *J. Phys. Chem. B.* **2006**, *51*, 26089-26097.

(18) Tyrode, E.; Johnson, C. M.; Rutland, M. W.; Day, J. P. R.; Bain, C. D. *J. Phys. Chem. C.* **2007**, *111*, 316-329.

(19) Greenspan, L. *J. Res. Natl. Bureau Stand. A. Phys. Chem.* **1977**, *81A*, 89-96.

(20) Geer, R. E.; Stenger, D. A.; Chen, M. S.; Calvert, J. M.; Shashidhar, R.; Jeong, Y. H.; Pershan, P. S. *Langmuir* **1994**, *10*, 1171-1176.

(21) Kulinich, S. A.; Farzaneh, M. *Surf. Sci.* **2004**, *573*, 379-390.

(22) Wu, K.; Bailey, T. C.; Willson, C. G.; Ekerdt, J. G. *Langmuir* **2005**, *21*, 11795-11801.

(23) Moulder, J. F.; Stickle, W. R.; Sobol, P. E.; Bomben, K. D. *Handbook of X-ray photoelectron spectroscopy: A reference book of standard spectra for identificiation and interpretation of XPS data.* Physical Electronics: Eden Prairie, MN, 1992.

(24) Wang, J.; Paszti, Z.; Even, M. A.; Chen, Z. *J. Am. Chem. Soc.* **2002**, *124*, 7016-7023.

(25) Lenk, T. J.; Hallmark, V. M.; Hoffman, C. L.; Rabolt, J. F.; Castner, D. G.; Erdelen, C.; Ringsdor, H. *Langmuir* **1994**, *10*, 4610-4617.

(26) Masetti, G.; Cabassi, F.; Morelli, G.; Zerbi, G. *Macromolecules* **1973**, *6*, 700-707.

(27) Lee, S. H.; Wang, J.; Krimm, S.; Chen, Z. *J. Phys. Chem. A* **2006**, *110,* 7035-7044.

(28) Wang, J.; Lee, S. H.; Chen, Z. *J. Phys. Chem. B* **2008**, *112,* 2281-2290.

(29) Chen, X.; Wang, J.; Boughton, A. P.; Kristalyn, C. B.; Chen, Z. *J. Am. Chem. Soc.* **2007**, *129,* 1420-1427.

(30) Nguyen, K.; Le Clair, S.; Ye, S.; Chen, Z., *J. Phys. Chem. B* **2009**, *113*, 12169-12180.

(31) Carraro, C.; Oranna, W.; Sung, M. M.; Maboudian, R. *J. Phys. Chem. B* **1998**, *102*, 4441-4445.

CHAPTER 5: SURFACE PARA-SUBSTITUTED PHENYL GROUP ORIENTATION PROBED BY SUM FREQUENCY GENERATION VIBRATIONAL SPECTROSCOPY

5.1 INTRODUCTION

The materials discussed previously in Chapter 2 contained both polystyrene and pyridinium portions, which are respectively a mono-substituted and para-substituted ring structure. Both groups can likely generate aromatic C-H stretching signals. Mono-substituted ring orientation on surfaces and at interfaces has been determined using SFG in previous works,[1-4] however little work has been done to examine para-substituted ring orientation. To better characterize the polymers investigated in Chapter 2 it was decided to develop orientation analysis method to accurately examine such para-substituted rings. For this purpose, sulfonated polystyrene (PSS) was studied (Figure 5.1). PSS was examined with a sodium ion as the counter ion as well as the commercial mixture of PSS and poly(3,4-ethylenedioxythiophene) (PEDOT) (Figure 5.1) known as Baytron P.

Baytron P contains a significant amount of PSS. The presence of PEDOT should not confuse the collected SFG data in the aromatic C-H stretching frequency region as there is no aromatic C-H group in PEDOT. In the past, the orientation of phenyl groups on a polystyrene (PS) surface has been investigated using SFG.[1-3] However, PSSNa is a para-substituted ring system while PS is a mono-substituted ring. Here a method has been applied to study the para-substituted phenyl groups to determine the orientation of the phenyl groups on the PSSNa surface. After the PSSNa surface was analyzed, the PSS phenyl ring orientation at the Baytron P surface was determined.

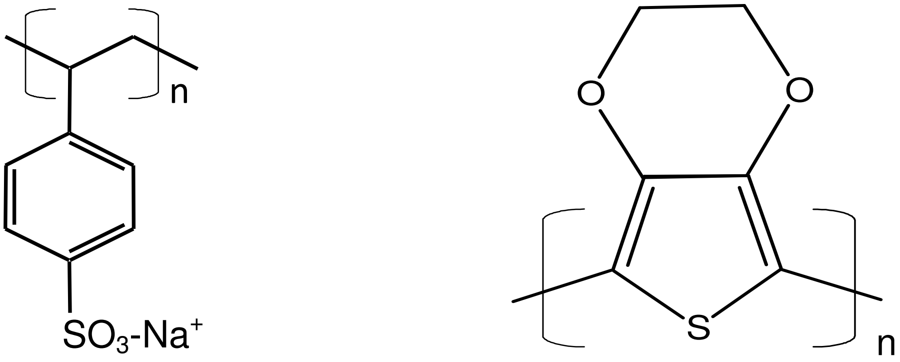

Poly(sodium 4-styrenesulfonate) (PSSNa)   poly(3,4-ethylenedioxythiophene) (PEDOT)

Figure 5.1. Molecular formula for poly(sodium 4-styrenesulfonate) (PSSNa) and Poly(3,4-ethylenedioxythiophene) (PEDOT).

5.2 EXPERIMENTAL

5.2.1 Sample Preparation

The Baytron P sample with 1:2.5 poly(3,4-ethylenedioxythiophene) (PEDOT):poly(sodium 4-styrenesulfonate) (PSS) was obtained from H. C. Starck. Poly(sodium 4-styrenesulfonate) (PSSNa) was purchased from Acros Organics. All chemicals were used as received. Polymer films were spin coated from 2% wt/wt solution of poly(sodium 4-styrenesulfonate) in de-ionized water on calcium fluoride at 2500 rpm. Baytron P was spin coated on calcium fluoride windows at 4200 rpm.

5.2.2 SFG

The experimental SFG set-up, SFG theory, and SFG experimental geometry have been covered in Chapter 1. In this research, a face-down window geometry was adopted. For the PSSNa sample, the input visible energy was ~100 μJ in the SFG experiment. For the Baytron P sample, the input visible energy was reduced to ~50 μJ, to minimized degradation from the Baytron P.

5.3 RESULTS AND DISCUSSION

5.1 General discussion of SFG spectra

SFG spectra were collected from surfaces of PSSNa and Baytron P samples. The spectra will be discussed and analyzed in more detail below. First the aromatic C-H vibrational modes of PSSNa will be examined. As discussed previously, the phenyl group in PS is a mono-substituted aromatic ring. There are five normal modes for the aromatic C-H stretching vibrations for such a phenyl group,[5,6] as depicted in Figure 5.2. The phenyl group symmetry belongs to a C_{2v} point group, thus all the five modes are both IR and Raman active. Only when a vibrational mode is both IR and Raman active, can it be detected in SFG. Therefore all five modes are SFG active.

The SFG hyperpolarizability tensor, β, can be described as a tensor product of the IR transition dipole moment and the Raman polarizability tensor.[7]

$$\beta_{lmn,q} \propto \frac{\partial \alpha^{*}_{lm}}{\partial Q_q} \frac{\partial \mu_n}{\partial Q_q} \qquad (5.1)$$

where l, m, and n are the molecular coordinates, $\frac{\partial \alpha_{lm}}{\partial Q_q}$ and $\frac{\partial \mu_n}{\partial Q_q}$ are the Raman polarizability and IR dipole moment derivatives with respect to the normal mode coordinate of the q^{th} vibrational mode, respectively. A vibrational mode with both strong IR and Raman signals may lead to a strong SFG signal. For the five modes depicted in Figure 5.2, the ν_2 and ν_{7a} modes can have both large IR transition dipole moment and

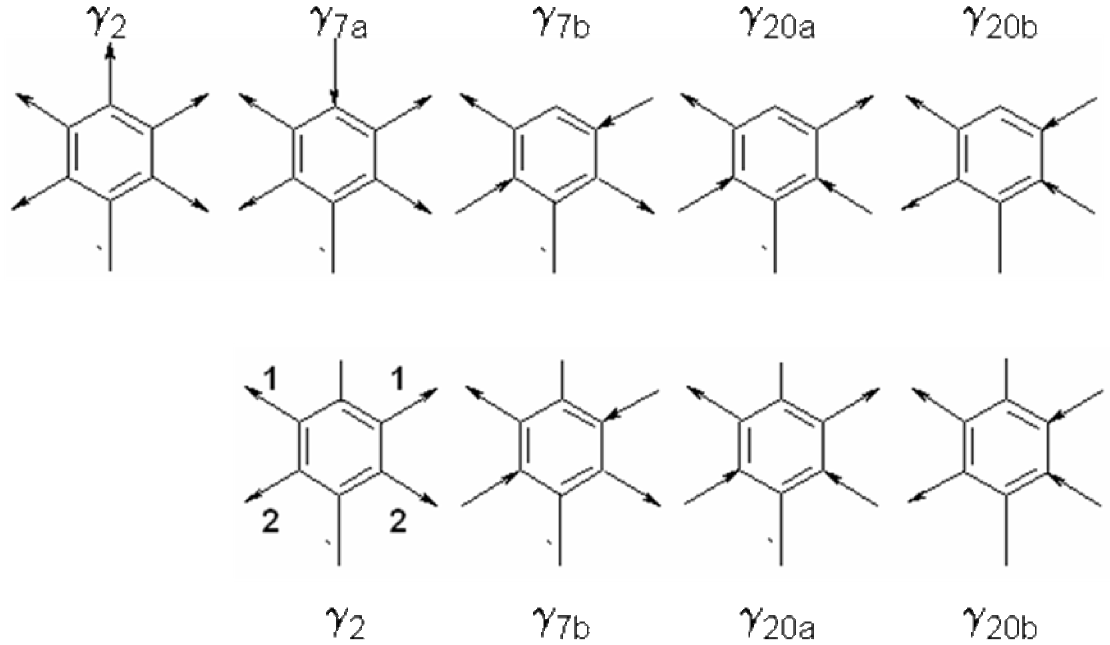

Figure 5.2. The five normal modes of the C-H stretching vibrations for a mono-substituted phenyl ring and the four normal modes for a para-substituted phenyl ring.

Raman polarizability, therefore they may have strong SFG signals. This also depends on the beam polarization combinations used to collect the signal.

Clearly, the SFG activity for the ν_{7b} mode depends on the "unequal" IR dipole transition moment derivatives of the C-H bonds at the ortho and meta positions from the mono-substituted position. If these two positions are the same, this mode is IR forbidden. If these two positions are not drastically different (e.g., for PS), ν_{7b} mode may generate weak IR signal, leading to a weak SFG signal as well. The SFG activities for the ν_{20a} and ν_{20b} modes depend on the "unequal" Raman polarizability derivatives of the C-H bonds at the ortho and meta positions from the mono-substituted position. Similarly, if these two positions are not drastically different, these two modes generate weak Raman signals, leading to weak SFG signals. According to this analysis, SFG signals of the ν_2 and ν_{7a} modes are likely dominating.

Different from the PS phenyl group, which is mono-substituted, the PSSNa aromatic ring is para-substituted. Because the two substitutions are not the same, the group (still called phenyl in this work) has a C_{2v} symmetry as well. For the phenyl group in PSSNa, the two PS modes ν_2 and ν_{7a} become the same. This new mode is called ν_2. It is both IR and Raman active because of the hetero-substitution, creating "unequal" positions in the carbon 1 and carbon 2 within the group (Figure 5.2). The ν_2 and ν_{7b} modes are IR active because of the hetero-substitution. Since ν_2 mode has a stronger Raman signal than ν_{7b} mode does, ν_2 mode may lead to a stronger signal in SFG spectrum. Similar to the ν_{20a} and ν_{20b} modes in PS, their PSSNa intensities must also depend on how strongly the hetero-substitution affects the Raman polarizabilities of the C-H bonds at the carbon 1 and carbon 2 positions.

Figure 5.3 shows the surface SFG spectra of PSSNa, and Baytron P collected using the ssp and sps polarization combinations. Such SFG spectra were fitted using the following equation:

$$\chi_{eff}^{(2)} = \chi_{nr} + \sum \frac{A_q}{\omega_{IR} - \omega_q + i\Gamma_q} \tag{5.2}$$

where $\chi_{eff}^{(2)}$ is the effective second-order nonlinear susceptibility, $\chi_{nr}^{(2)}$ is the nonresonant background and A_q, ω_q, and Γ_q are the strength, resonant frequency and damping coefficient (width) for the vibrational mode q. The SFG spectral assignment and fitting results are shown in Table 5.1. The peak assignment was based on the previous SFG study on the polar orientation of the benzoate derivative counterions bound to a surfactant

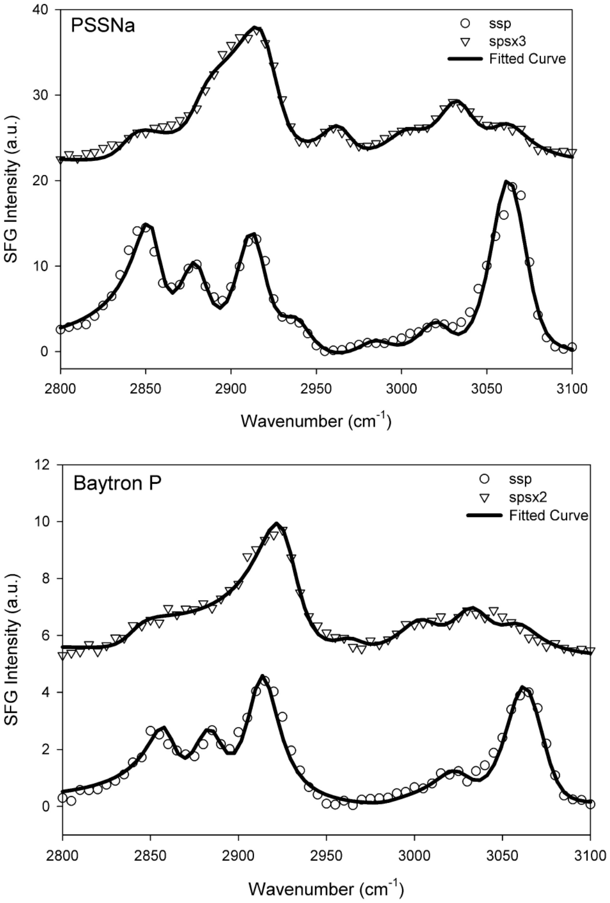

Figure 5.3. The ssp and sps SFG spectra of the PSSNa (top) and Baytron P (bottom) surfaces.

monolayer,[7] and the comprehensive reference book about IR and Raman peak assignment of benzene derivatives.[5,6] Indeed, the signal from the ν_2 mode in the ssp spectrum is the strongest signal for all samples. For the two samples, the intensities of ν_{7b}, ν_{20a} and ν_{20b} modes are relative weak and become more prominent only in the sps spectra.

5.2 Orientational order of the phenyl groups on surfaces

To determine the orientation information of the phenyl groups on a surface, it is necessary to know the relationship between the surface effective second-order nonlinear susceptibility and the molecular hyperpolarizability. The effective second-order nonlinear

Table 5.1. Fitting parameters for the surface SFG spectra of PSSNa and Baytron P. ss: symmetric stretching; as: anti-symmetric stretching; Fermi: Fermi resonance.

Sample	ω_q (cm^{-1})	A_q		Γ_q (cm^{-1})	Assignment
		ssp	sps		
PSSNa	2855	23±1	-11±1	10	CH$_2$ ss
	2881	26±1	-10±1	12	CH$_3$ ss
	2895	14±1	—	15	Unassigned
	2913	38±1	—	12	CH$_2$ Fermi
	2922	—	27±1	12	CH$_2$ as
	2938	15±1		12	CH$_3$ Fermi
	2965	—	9±1	12	CH$_3$ as
	3005	—	8±1	15	Combination
	3021	21±2	—	15	ν_{20b}
	3030	-6±1	18±1	15	ν_{7b}
	3060	73±2	12±1	15	ν_2
	3076	-30±1	—	15	ν_{20a}
Baytron P	2840	—	-5±1	10	Combination
	2860	9±1	—	10	CH$_2$ ss
	2885	13±1	—	12	CH$_3$ ss
	2895	-10±1	—	15	unassigned
	2913	23±1	—	12	CH$_2$ Fermi
	2927	—	19±1	15	CH$_2$ as
	2965	—	3±1	12	CH$_3$ as
	3005	—	7±1	15	Combination
	3025	12±1	—	15	ν_{20b}
	3034	-2±1	10±1	15	ν_{7b}
	3060	34±1	7±1	15	ν_2
	3076	-15±1	—	15	ν_{20a}

susceptibility, especially the ratio between certain components in the second-order nonlinear susceptibility can be measured in SFG experiments using different polarization combinations of the input and output beams. The hyperpolarizability components of the para-substituted phenyl groups can be calculated. The effective second-order nonlinear susceptibility is related to the hyperpolarizability through orientation angles of the surface functional groups; therefore such orientation information can be deduced.

As we discussed above, for a para- substituted phenyl ring, a local C_{2v} symmetry can be adopted for analysis. It is reasonable to assume that both sample surfaces are azimuthally isotropic and thus only the tilt angle and the twist angle of the phenyl ring to determine the orientation need to be considered. Figure 5.4 shows the schematic describing the laboratory-fixed and the molecule-fixed coordinates for a phenyl group adopting the C_{2v} symmetry. The molecule-fixed coordinate system is defined as an (a, b, c) system. The "c" axis is in the same direction as the principal axis of the C_{2v} symmetry; the "a" axis is perpendicular to the "c" axis and is in the phenyl plane; the "b" axis is orthogonal to the phenyl plane. The laboratory-fixed coordinate system is defined as an (X, Y, Z) system. The tilt angle θ is defined as the angle between the Z-axis (which is the surface normal) and the c-axis of the phenyl group. The twist angle ϕ is defined as the rotation angle of the phenyl plane with respect to the c-axis. Based on the local C_{2v} symmetry for the para-substituted phenyl rings, we know that ν_2, and ν_{20a} modes belong

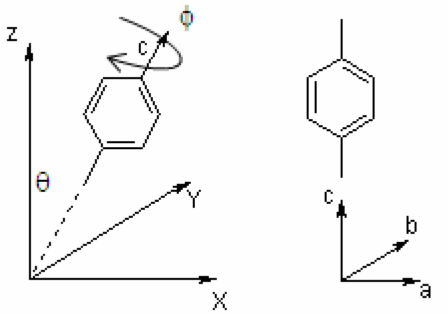

Figure 5.4. The schematic pictures show the laboratory-fixed coordinate (left) and the molecule-fixed coordinate (right), respectively.

to the A_1 irreducible representation, which has three non-zero molecular hyperpolarizability components: β_{aac}, β_{bbc}, and β_{ccc}. The ν_{7b} and ν_{20b} modes belong to the B_1 irreducible representation, which has two non-zero molecular hyperpolarizabilities, $\beta_{aca} = \beta_{caa}$. The relations between the second order nonlinear susceptibility components and various hyperpolarizability components for different modes are:[4,8-10]

For A1:

$$\begin{aligned}\chi_{yyz,A1} = \frac{N_s}{8}[&\beta_{aac,A1}\cos\theta\left(3+\cos 2\theta - 2\sin^2\theta\cos 2\phi\right) \\ &+ \beta_{bbc,A1}\cos\theta\left(3+\cos 2\theta + 2\sin^2\theta\cos 2\phi\right) + \beta_{ccc,A1}\left(\cos\theta - \cos 3\theta\right)]\end{aligned} \tag{5.3}$$

$$\begin{aligned}\chi_{yzy,A1} = \frac{N_s}{16}[&-\beta_{aac,A1}\left(\cos\theta - \cos 3\theta\right)\left(1+\cos 2\phi\right) - \beta_{bbc,A1}\left(\cos\theta - \cos 3\theta\right)\left(1-\cos 2\phi\right) \\ &+ 2\beta_{ccc,A1}\left(\cos\theta - \cos 3\theta\right)]\end{aligned} \tag{5.4}$$

For B1:

$$\chi_{yyz} = -\frac{N_s}{8}\beta_{aca}\left(\cos\theta - \cos 3\theta\right)\left(1+\cos 2\phi\right) \tag{5.5}$$

$$\chi_{yzy} = \frac{N_s}{8}\beta_{aca}\left[4\cos\theta - \left(\cos\theta - \cos 3\theta\right)\left(1+\cos 2\phi\right)\right] \tag{5.6}$$

As we mentioned above, the second order nonlinear optical susceptibility components especially their ratios can be measured in the SFG experiment. In order to deduce the tilt and twist angles, the relative hyperpolarizablity tensor component ratios in the above equations should be known. For para-substituted phenyl ring in PSSNa, we focused on the ν_2 and ν_{7b} modes. The bond-additivity approach was applied to evaluate the following relative hyperpolarizablity tensor component ratios.[7-11]

For para-substituted phenyl ring, we have:

$$\frac{\beta_{ccc,\nu 2}}{\beta_{aac,\nu 2}} = 0.69, \ \frac{\beta_{bbc,\nu 2}}{\beta_{aac,\nu 2}} = 0.04, \ \frac{\beta_{aca,\nu 7b}}{\beta_{aac,\nu 2}} = 0.47.$$

By combining the measured SFG spectra and the above deduced ratios, the tilt and twist angles can be determined. The different ratios will be used to cross check the accuracy of the deduced orientation angles.

The para-substituted phenyl groups tilt and twist angles at the PSSNa and Baytron P surfaces were estimated by inputting these deduced values into the above equations to relate χ and β. For the para-substituted phenyl ring:

$$\frac{\chi_{yyz,\nu 2}}{\chi_{yzy,\nu 2}} = \frac{25.4\cos\theta - \cos 3\theta - 11.3\cos\theta\sin^2\theta\cos 2\phi}{(\cos\theta - \cos 3\theta)(1 - 2.82\cos 2\phi)} \tag{5.9}$$

$$\frac{\chi_{yyz,\nu 7b}}{\chi_{yzy,\nu 7b}} = \frac{(\cos 3\theta - \cos\theta)(1 + \cos 2\phi)}{4\cos\theta - (\cos\theta - \cos 3\theta)(1 + \cos 2\phi)} \tag{5.10}$$

$$\frac{\chi_{yyz,\nu 7b}}{\chi_{yyz,\nu 2}} = \frac{(\cos 3\theta - \cos\theta)(1 + \cos 2\phi)}{9.21\cos\theta - 0.36\cos 3\theta - 4.43\cos\theta\sin^2\theta\cos 2\phi} \tag{5.11}$$

$$\frac{\chi_{yzy,\nu 7b}}{\chi_{yzy,\nu 2}} = \frac{4\cos\theta - (\cos\theta - \cos 3\theta)(1 + \cos 2\phi)}{(\cos\theta - \cos 3\theta)(0.36 - 1.02\cos 2\phi)} \tag{5.12}$$

By combining any of the two equations among the above four equations, both the tilt angle and the twist angle can be deduced. A tilt angle assuming an isotropic distribution of the twist angle was also determined. The results are shown in Table 5.2 and Table 5.3 for the PSSNa and Table 5.4 and Table 5.5 for Baytron P.

When different combinations of the two equations are used, the deduced tilt angle and the twist angle are similar, showing the reliability of the deduced angles. Table 5.2 shows that the averaged tilt and twist angles of the phenyl groups at the PSSNa surface are 47.5°±5.3° and 58.8°±8.2°, respectively. However, the tilt angles deduced from

Table 5.2. The deduced tilt and twist angles of the phenyl groups at the PSSNa surface.

No.	Tilt angle (°)	Twist angle (°)	Sources
1	51	52	$\chi_{yyz,v2}/\chi_{yzy,v2}$ $\chi_{yyz,v7b}/\chi_{yzy,v7b}$
2	48	61	$\chi_{yyz,v2}/\chi_{yzy,v2}$ $\chi_{yzy,v7b}/\chi_{yzy,v2}$
3	48	64	$\chi_{yyz,v7b}/\chi_{yzy,v7b}$ $\chi_{yzy,v7b}/\chi_{yzy,v2}$
4	43	58	$\chi_{yyz,v7b}/\chi_{yyz,v2}$ $\chi_{yzy,v7b}/\chi_{yzy,v2}$
Averaged	47.5±5.3	58.8±8.2	------------

Table 5.3. The deduced tilt angle of the phenyl groups at the PSSNa surface supposing an isotropic twist. *exceeds predicted ratio

No.	Tilt angle (°)	Source
1	Out of range, near 90° *	$\chi_{yyz,v2}/\chi_{yzy,v2}$
2	32	$\chi_{yyz,v7b}/\chi_{yzy,v7b}$
3	25	$\chi_{yyz,v7b}/\chi_{yyz,v2}$
4	63	$\chi_{yzy,v7b}/\chi_{yzy,v2}$

Table 5.4. The deduced tilt and twist angles of the phenyl groups at the Baytron P surface.

No.	Tilt angle (°)	Twist angle (°)	Sources
1	50	62	$\chi_{yyz,v2}/\chi_{yzy,v2}$ $\chi_{yyz,v7b}/\chi_{yzy,v7b}$
2	49	66	$\chi_{yyz,v2}/\chi_{yzy,v2}$ $\chi_{yzy,v7b}/\chi_{yzy,v2}$
3	49	68	$\chi_{yyz,v7b}/\chi_{yzy,v7b}$ $\chi_{yzy,v7b}/\chi_{yzy,v2}$
4	45	65	$\chi_{yyz,v7b}/\chi_{yyz,v2}$ $\chi_{yzy,v7b}/\chi_{yzy,v2}$
Averaged	48.2±3.6	65.2±4.0	------------

Table 5.5. The deduced tilt angle of the phenyl groups at the Baytron P surface supposing an isotropic twist. *exceeds predicted ratio

No.	Tilt angle (°)	Source
1	Out of range, near 90° *	$\chi_{yyz,v2}/\chi_{yzy,v2}$
2	26	$\chi_{yyz,v7b}/\chi_{yzy,v7b}$
3	21	$\chi_{yyz,v7b}/\chi_{yyz,v2}$
4	54	$\chi_{yzy,v7b}/\chi_{yzy,v2}$

different equations assuming an isotropic (or random) distribution of the twist angle using different combinations of the two equations are quite different, as shown in Table 5.3. Clearly, the PSSNa phenyl groups do not have an isotropic twist angle distribution. It appears that the PSSNa phenyl groups adopt a specific orientation with certain tilt and twist angles.

The average tilt angle and twist angle of PSS component within Baytron P were also determined. Again tilt and twist angle results in Table 5.4 do not differ significantly. The two angles are 48.2°±3.6° and 65.2°±4°, respectively. The PSS tilt angle within Baytron P surface is similar to PSSNa, but the twist angle is slightly different, possibly due to the interactions between the PSS and PEDOT in Baytron P. Similar to the PSSNa situation, the Baytron P phenyl tilt angles were found to be very different using different combinations of the two equations and assuming an isotropic or random distribution of the twist angle (Table 5.5), indicating that the PSS phenyl groups within Baytron P do not have an isotropic twist angle.

5.4 CONCLUSIONS

SFG was applied to deduce phenyl group orientation for PSSNa and Baytron P surfaces. For the PSSNa para-substituted phenyl ring a tilt angle of 47.5°±5.3° and a twist angle of 58.8°±8.2° were found. The phenyl groups in Baytron P on the surface exhibit tilt and twist angles of 48.2°±3.6° and 65.2°±4.0° respectively, indicating the orientations are not very different. The similarity in both the tilt and twist angles of phenyl groups on the PSSNa and Baytron P surfaces was to be expected because a significant portion of the signal likely resulted from the excess PSSNa (1 PEDOT: 2.5 PSSNa) present in Baytron P. Some differences between PSSNa and Baytron P phenyl twist angle values could be attributed to the fact that some of PSSNa in Baytron P interacts electrostactically with PEDOT, affecting the phenyl ring orientation.

5.5 REFERENCES

(1) Briggman, K. A.; Stephenson, J. C.; Wallace, W. E.; Richter, L. J. *J. Phys. Chem. B* **2001**, *105*, 2785-2791.

(2) Gautam, K. S.; Schwab, A. D.; Dhinojwala, A. *Phys. Rev. Lett.* **2000**, *85*, 3854-3857.

(3) Chen, C.; Wang, J.; Woodcock, S. E.; Chen, Z. *Langmuir* **2002**, *18*, 1302-1309.

(4) Chen, C.; Wang, J.; Even, M. A.; Chen, Z. *Macromolecules* **2002**, *35*, 8093-8097.

(5) Varsanyi, G. *Assignments for Vibrational Spectra of Seven Hundred Benzene Derivatives: Vol. 1*; Halsted Press: New York, 1974.

(6) Varsanyi, G. *Vibrational Spectra of Benzene Derivatives*; Academic Press: New York and London, 1969.

(7) Duffy, D. C.; Davies, P. B.; Bain, C. D. *J. Phys. Chem.* **1995**, *99*, 15241-15246.

(8) Hirose, C.; Akamatsu, N.; Domen, K. *Appl. Spectrosc.* **1992**, *46*, 1051-1072.

(9) Hirose, C. K.; Akamatsu, N.; Domen, K. *J. Chem. Phys*. **1992**, *96*, 997-1004.

(10) Hirose, C.; Yamamoto, H.; Akamatsu, N.; Domen, K. *J. Phys. Chem.* **1993**, *97*, 10064-10069.

CHAPTER 6: SUMMARY AND CONCLUSIONS

The research focus of this work is to better understand the behavior of polymer surfaces for the use as marine anti-fouling coatings. Through the use of sum frequency generation vibrational spectroscopy, the surface properties of several anti-fouling polymers have been explored in various environments, including air and water. Various experimental geometries were adopted and several vibrational modes were examined. Polymer composition was found to have an effect on the interaction between the polymer and a model cell membrane, a lipid bilayer. The SFG results also show that the polymer surfaces restructure rapidly when shifted from a hydrophobic air environment to a hydrophilic aqueous environment. Vibrations in the C-H and C-F stretching frequency regions were observed using SFG. In order to better understand the C-F stretches detected, a model self assembled thin layer with fluorinated functional groups was investigated to examine the peak assignments for C-F stretches. Further attempts to understand the structure of the anti-fouling polymers centered on the examination of the para-substituted phenyl groups. In this study, sulfonated polystyrene was investigated by SFG to develop the data analysis method to determine phenyl orientation from polarized SFG spectra. Many polymers being developed for marine anti-fouling coating contain aromatic rings. The results can be applied to understand surface structures of these polymers in further detail in the future.

SFG was used to examine the interaction of several anti-fouling polymers with model cell membranes by mixing them with lipids to prepare lipid bilayers. It was shown that the presence of a fluorinated portion in the polymer significantly affects the behavior of the polymer and results in a different rate of interaction with the lipid bilayer compared to similar solely alkylated polymers. To fully understand these behavior SFG spectra were collected from these polymer surfaces in air and D_2O using a face-down window geometry. However, the SFG signals from the polymer/D_2O interface were too weak when a fused silica was used as the substrate. To enhance SFG signal, a total reflection prism geometry was adopted in the experiment. Comparison between the spectra collected using the window and prism geometry in air indicates significant differences. Likely, the signal collected using the prism geometry was resultant from more than just the polymer/air interface and included either bulk signals or buried polymer/substrate interface signals.

With this knowledge in hand, a thickness dependence study using prism geometry was undertaken on a new anti-fouling polymer. It was observed for both the polymer/air and polymer/D_2O interfaces that the observed SFG signals changed as the thickness of the polymer thin film changed. Utilizing the Fresnel coefficients of both the polymer/air (D_2O) and buried prism/polymer interfaces, it was shown that the polymer/air (D_2O) interfaces dominate. It was also observed that as the polymer film thickness increased the SFG signal contributed from the buried polymer/substrate interface could interfere with that from the polymer/air interface, resulting in the decrease in total detected SFG signal. Similarly, it was also found that the signal from the buried polymer/substrate interface interfered with that from the polymer/D_2O interface. Further examination of the anti-fouling polymer in the C-F stretching frequency region showed that C-F stretching mode could be observed in both air and aqueous environments. Therefore as designed, the fluorinated portion of the polymer is still present at the surface even upon contacted with an aqueous environment. However, the detailed peak assignment for C-F stretches was still unclear.

To further understand the observed SFG signals from the C-F vibrational modes, a simple partially fluorinated silane was chosen to form a self assembled thin layer. Ideally, this system should form a well ordered highly packed monolayer that would be ideal for use as a model to examine C-F SFG signals. However, characterization by contact angle goniometry, ellipsometry, and XPS revealed that the systems in study were less than ideal. Depending on the sample deposition time it was observed that both the amount of material and orientation of the molecules in silane thin film would change. For very short deposition times, combined SFG and XPS results showed that the surface coverage of the silane was very low, and the orientation of the silane was different from that observed from longer deposition times. At longer deposition times it was found that material was still being deposited even past the point where an ideal monolayer would have formed. However, this increase in material was only reflected slightly in the corresponding SFG spectra. Treatment of the fluorinated silane as a partial helix showed that if the observed C-F signal arose from the CF_2 axial stretch as commonly assigned in SAMs literature the only observable SFG signal should occur in the sps polarization. As no signal was detected in sps, this assignment is unlikely correct. The other possible assignment to the CF_3 asymmetric mode was supported by FTIR studies done on a short silane with only a CF_3 terminus and no CF_2 groups present. Based on this assignment, no orientation information can be determined, so the overall orientation of the silane cannot be determined by SFG.

Another aspect of understanding the anti-fouling polymers revolved around trying to better understand the orientation of the phenyl groups present in several of the polymers. Using sulfonated polystyrene, the data analysis method to determine orientation of phenyl groups from polarized SFG spectra was developed, which can be applied to study anti-fouling polymer surface structures in the future. It was found that for a para-substituted phenyl ring, the assumption of isotropic twist is not valid and results in a wide range of tilt angles for the phenyl group determined using different polarized spectra. Inclusion of the twist angle in the determination of orientation results in very good agreement between various measurements.

The methodology developed in this thesis to study polymer surfaces and interfaces by varying polymer film thicknesses will be useful for future studies on other anti-biofouling polymers. The knowledge on C-F stretches obtained in this work will also help the future studies on fluorinated polymers. Future experiments that could be performed include examining the interaction of anti-fouling polymers with various protein solutions to observe conformation changes in both the protein and the polymer at the interface. Such studies will provide further understanding on biofouling because the first step for biofouling to occur is the interactions between adhesive proteins from marine organisms and the polymer coating. While this thesis work has not completely elucidated the behavior of anti-fouling polymers, it is a significant step in providing a frame work for future experiments with new materials.